JGR Atmospheres

RESEARCH ARTICLE
10.1029/2020JD034027

Key Points:

- Airborne observations in tropical cyclones successfully force a nonlinear boundary layer model to simulate meaningful response features
- A broadened wind field prior to secondary eyewall formation (SEF) produces an updraft maximum associated with an incipient secondary eyewall
- The updraft maximum is strongest left of the shear vector, suggesting that this region plays an early role in SEF

Correspondence to:
A. C. Didlake, Jr.,
didlake@psu.edu

Citation:
Yu, C.-L., Didlake, A. C. Jr., Kepert, J. D., & Zhang, F. (2021). Investigating axisymmetric and asymmetric signals of secondary eyewall formation using observations-based modeling of the tropical cyclone boundary layer. *Journal of Geophysical Research: Atmospheres*, *126*, e2020JD034027. https://doi.org/10.1029/2020JD034027

Received 8 OCT 2020
Accepted 11 JUL 2021

Investigating Axisymmetric and Asymmetric Signals of Secondary Eyewall Formation Using Observations-Based Modeling of the Tropical Cyclone Boundary Layer

Chau-Lam Yu[1,2], Anthony C. Didlake Jr.[1], Jeffrey D. Kepert[3], and Fuqing Zhang[1,2]

[1]Department of Meteorology and Atmospheric Science, The Pennsylvania State University, University Park, PA, USA, [2]Center for Advanced Data Assimilation and Predictability Techniques, The Pennsylvania State University, University Park, PA, USA, [3]Bureau of Meteorology, Melbourne, VIC, Australia

Abstract This study examines axisymmetric and asymmetric aspects of secondary eyewall formation (SEF) in tropical cyclones (TCs) by applying a nonlinear boundary layer model to tangential wind composites of observed TCs with and without SEF. SEF storms were further analyzed at times prior to and after SEF, as defined by the emergence of a secondary maximum in axisymmetric tangential wind. The model is used to investigate the steady-state boundary layer response to the free-tropospheric pressure forcing derived from observed tangential wind fields. The axisymmetric response to the Post-SEF wind field displayed a secondary updraft maximum associated with a mature secondary eyewall; the model correctly produced no secondary updraft for non-SEF storms. The Pre-SEF response also exhibited a secondary updraft associated with an incipient secondary eyewall largely due to the broadened outer tangential wind field that commonly precedes SEF events. The asymmetric wind fields and model response were analyzed relative to the 850–200 hPa environmental wind shear vector. In Pre-SEF storms, the tangential wind field displayed a broadened tangential wind structure in the downshear quadrants. The boundary layer response shows a downwind shift toward the left-of-shear quadrants, exhibiting the clearest secondary maxima in updrafts, tangential wind, and radial inflow. This left-of-shear response was the leading contributor to the secondary eyewall signals in the Pre-SEF axisymmetric response. Sensitivity analyses confirmed the robustness of these asymmetric signals. These findings suggest that enhanced tangential wind and boundary layer updrafts in the left-of-shear sectors may be early indicators and critical features of SEF in sheared TCs.

Plain Language Summary SEF in TCs marks the beginning of an eyewall replacement cycle, a process that has impacts on the storm intensity and structure. The initiation of the SEF process is generally not well-forecasted or fully understood. This study uses airborne observations and a nonlinear numerical model to examine the role of the boundary layer during SEF. We find that the earliest boundary layer signs of SEF are clearest in the left-of-shear sectors. We also show that these early left-of-shear signals of SEF are robust and systematically stronger than that of the other sectors, indicating that these sectors are the preferred location where initiation of SEF repeatedly occurs in these observed cases. The results of this study provide new insight to the evolution of TCs and can be potentially used for improving TC forecasts.

1. Introduction

Secondary eyewall formation (SEF) is an inner-core process that occurs in some mature tropical cyclones (TCs) and can cause significant intensity and structural changes of the storm (Black & Willoughby, 1992; Willoughby et al., 1982). Despite the frequent occurrence of SEF (Hawkins et al., 2006), the underlying physical mechanisms for SEF have yet to be fully determined. Previous studies have hypothesized that certain dynamical features are important for SEF, including outward-propagating vortex-Rossby waves (VRWs) (Guimond et al., 2020; Menelaou et al., 2012; Montgomery & Kallenbach, 1997), convectively generated potential vorticity anomalies from inward-spiraling rainbands (Judt & Chen, 2010; Qiu et al., 2010), an enhanced background vorticity radial gradient (Abarca & Corbosiero, 2011; Terwey & Montgomery, 2008), and a region of rapid filamentation that supports the formation of a precipitation-free moat outside a primary eyewall (Rozoff et al., 2006; H. Wang et al., 2019; Y. Wang, 2008).

Previous modeling studies have also explored the role of axisymmetric boundary layer processes in SEF. Several studies have shown that SEF occurs in association with the development of enhanced supergradient flow in the upper boundary layer (Abarca & Montgomery, 2013, 2014; Abarca et al., 2015; Huang et al., 2012; Wu et al., 2012). These studies make a connection between outwards acceleration in the supergradient flow region and horizontal convergence, leading to an updraft which can lead to SEF. Alternatively, Kepert (2013) showed that, using a nonlinear steady-state model of the TC boundary layer developed by Kepert and Wang (2001; hereafter the KW01 model), significant outer updrafts could be produced by frictional convergence collocated with locally strong radial vorticity gradients in the cyclone's gradient wind field. The flow adjustment in this area also produced a region of supergradient flow in the upper boundary layer. He further proposed a hypothesis that a positive feedback between frictional convergence, convection, and vortex-tube stretching could contribute to SEF. Using the full-physics Weather Research and Forecasting (WRF) model, Kepert and Nolan (2014) and F. Zhang et al. (2017) later explored these ideas and showed that the simulated response from the KW01 model agrees well with the boundary layer evolution of the WRF simulations, including a realistic representation of the secondary eyewall updraft.

Many of the previously mentioned theories require some pre-existing vorticity anomaly outside of the eyewall to modulate or initiate a certain axisymmetric dynamical mechanism, where this vorticity anomaly is generated by rainband convection. On the other hand, the VRW SEF theory does not require such pre-existing rainband convection, but rather the source of vorticity comes from the inner core in the form of outward-propagating filaments (convectively coupled VRWs), as discussed by Fischer et al. (2020) and Guimond et al. (2020). To investigate the dynamical coupling between rainband and boundary layer processes, Kepert (2018, K18 hereafter) modified the KW01 model (hereafter the K18 model) to incorporate the nonlinear balanced pressure field corresponding to an asymmetric vorticity forcing that represents the forcing of a spiral rainband, and examined the asymmetric, steady-state boundary layer response to the rainband forcing. He showed that the boundary layer response to an asymmetric rainband vorticity forcing is structurally similar to that of an annular vorticity forcing representing a secondary eyewall, which strongly suggests a close dynamical linkage between rainbands and secondary eyewalls.

The K18 model (a modified KW01 model) has demonstrated its usefulness as a tool to understand the steady-state boundary layer response to simulated TC circulations during the SEF process. But this model has yet to be tested with actual TC observations. The current study performs these tests with the goal of uncovering new insight to SEF in real storms.

Wunsch and Didlake (2018, hereafter WD18) examined SEF in a composite analysis of aircraft 700 hPa level observations from 17 yr of Atlantic basin TCs. They showed that storms prior to SEF exhibited an axisymmetric broadening of the outer tangential wind field. This broadened wind field has commonly been identified as a precursor to SEF in observational studies (Bell et al., 2012; Didlake & Houze, 2013; Sitkowski et al., 2011) and modeling studies (Rozoff et al., 2006, 2012; Sun et al., 2013; Tang et al., 2017; Wang et al., 2016, 2019). Furthermore, WD18 showed that storms prior to SEF experience the largest change of the tangential wind field in the storm quadrants left of the 850–200 hPa environmental wind shear vector. This finding aligns with previous studies identifying a mesoscale descending inflow (MDI) pattern in left-of-shear stratiform rainbands that locally accelerates the tangential wind field prior to SEF (Didlake & Houze, 2013; Didlake et al., 2018; Yu et al., 2021). Given these results, WD18 hypothesized that the evolution of these wind-shear-induced asymmetries were indicative of recurring asymmetric rainbands that initiate SEF.

Building upon the results from WD18 and other previous studies, this study uses the K18 model to examine the steady-state boundary layer response to the tropospheric forcing represented by the observational composites of WD18. Both axisymmetric mean and asymmetric forcings are used to investigate how the boundary layer responds to the free tropospheric forcing aloft during SEF events and within storms without SEF. As emphasized in K18, since the nonlinear K18 model simulates the steady-state boundary layer response under the steady pressure forcing above the boundary layer, the result is only a one-way response of an apparent two-way interaction. However, because no feedback to the imposed tropospheric forcing is included in the model, the one-way frictionally driven updraft response in the boundary layer can therefore be isolated from an apparent two-way interaction in the coupling between the troposphere and boundary layer processes. The intent of our analysis is not to emphasize any particular SEF theory (e.g., Abarca &

Montgomery, 2013; Huang et al., 2012; Kepert, 2013; Miyamoto et al., 2018; Rozoff et al., 2006; Terwey & Montgomery, 2008; F. Zhang et al., 2017), nor to fully determine the forcing mechanism of an incipient secondary eyewall updraft. But rather, we used the K18 model as a skillful tool to examine where the earliest SEF-like structures might develop in the boundary layer and contribute most strongly to the azimuthal mean SEF signal, if one develops, based on the observed tangential wind composites. This analysis will help improve understanding of the axisymmetric and asymmetric structures and processes that are conducive to secondary eyewall development.

The remaining parts of the article is organized as follows. Section 2 introduces the K18 model used in this study, the data sets for each of the three SEF groups, and the preprocessing steps, as well as the forcings used to drive the model simulations. Section 3 first discusses the axisymmetric features simulated using the axisymmetric mean forcing, which is then followed by an analysis of the asymmetric response in a shear-relative framework, together with sensitivity analyses to examine the robustness and variability of these asymmetric features across the quadrants. Section 4 summarizes the conclusions of the study.

2. Data and Methodology

2.1. The K18 Model

To examine the boundary layer response to the observed free tropospheric wind distribution before and after SEF, we use the nonlinear boundary layer model developed by Kepert and Wang (2001) and later modified by Kepert (2018, the K18 model). The K18 model simulates the steady-state boundary layer response by integrating a set of prognostic three-dimensional nonlinear primitive equations to a near steady state. The model is dry and is forced by the pressure forcing from the free-tropospheric wind at the top of the integration domain, which is assumed to be above the boundary layer and is held constant in time. Since no feedback to the forcing field is included in the model, the simulated response is a one-way response of the boundary layer to the free tropospheric forcing. This simulated response includes boundary layer updrafts that are purely driven by frictional convergence. If moist processes were included in this same model, we would expect that the additional buoyancy effects would produce stronger updrafts. Different from the axisymmetric KW01 model, the pressure forcing used in the K18 model top can be either axisymmetric or asymmetric. Throughout this study, we use the word "asymmetric" to describe a field or simulation that includes non-axisymmetric features as part of the overall structure, as opposed to being purely asymmetric in the sense that only perturbations to the azimuthal mean are described. When axisymmetric forcing is used, the simulated result is equivalent to the KW01 model. When asymmetric forcing is used, it allows the investigation of the boundary layer response to cyclone asymmetries induced by environmental influences, such as environmental wind shear. This pressure forcing is implicitly represented by the gradient wind assumption in the axisymmetric mode and by a nondivergent wind in the asymmetric case through a nonlinear balance relation (see Equation 10 of K18). The procedures of deriving this asymmetric nondivergent wind field will be discussed in Section 2.3. More details of the model design can be found in K18.

The momentum equations in the K18 model include the horizontal and vertical momentum diffusion terms, which can be parameterized by various schemes. Kepert (2012) tested several commonly used boundary layer schemes and found that the Louis (Louis et al., 1982) and the Mellor-Yamada (Mellor & Yamada, 1982) schemes both produce a realistic hurricane boundary layer structure. Following the recommendation of Kepert (2012), the neutral Louis boundary layer scheme is used in the K18 model to parameterize momentum diffusion. The model has 20 vertical levels, covering from 10 m near the surface to 2.25 km. The maximum vertical spacing is 200 m and the horizontal grid spacing is 3 km. All experiments are integrated for 48 h to a nearly steady state.

2.2. Tangential Wind Composite From WD18

WD18 used the Extended Flight-Level Data set for TCs (FLIGHT+; Vigh et al., 2016) to perform a composite analysis for Atlantic hurricanes at category 3 (49.6 m s^{-1} maximum winds) or higher from year 1999 to 2015. They first identified storms that underwent SEF and marked the SEF time at the first instance when the axisymmetric tangential wind radial profile exhibited a secondary wind maximum. The 700 hPa level flight legs are then selected, and divided into groups without, prior to, and after SEF (the "Non-SEF," "Pre-SEF,"

and "Post-SEF" groups). In order to accommodate the different storm sizes and flight leg coverages for the composite analysis, the flight legs of each group were normalized. For the "Non-SEF" group, the wind profiles are normalized by the radius of maximum wind (r_1, RMW). For the Pre-SEF and Post-SEF groups, the flight legs were normalized by two length scales. For radii less than the RMW, the wind profile was normalized by the RMW (r_1), while outside the RMW, the wind profile was normalized by the width of the moat (m), which is defined as the distance between the primary and secondary tangential wind maxima in the observed tangential wind profiles (Wunsch & Didlake, 2018). The radius of the secondary maximum wind (r_2) is equal to $r_1 + m$. More detailed descriptions of the data set and the normalization procedure can be found in WD18.

In order to convert the normalized azimuthal mean composite wind profiles into input for the K18 boundary layer model, the following preprocessing steps are performed. First, each normalized flight legs are rescaled back to physical space using the median values of r_1 and r_2 of each group (only r_1 is used for Non-SEF group). Then, for the inner core region ($r < r_1$ = RMW), the legs were linearly interpolated to zero due to incomplete coverage of the flight legs. Individual legs that terminated at $r < 150$ km were removed from the composites to ensure that unphysical signals due to data unavailability were not displayed in the composite. The wind composites at large radii ($r > 150$ km) become noisy as the sample size drops at these large radii. Therefore, to provide a reasonable wind structure across the whole model domain, the wind profiles at $r > 150$ km are replaced by $Cr^{-0.5}$, where C is a constant to ensure continuity at the extrapolation radii. Figures 1a and 2a show the resulting azimuthal mean tangential wind and vorticity composites after the above rescaling procedure is performed, along with indicated locations of statistically significant differences (using the student's t test at the 95% confidence level) between each profile. The median values of r_1 and r_2 for each groups are shown in the legend of Figure 1a. Kepert (2017) shows that the nonlinear boundary layer dynamics exhibit an inherent low-pass filtering effect, which has length scale $l = -u_{10} / I$, where u_{10} is the radial wind at $z = 10$ m and $I = \sqrt{\left(2v / r + f\right)\left(1 / r\partial rv / \partial r + f\right)}$ is the inertia stability parameter, both of which are calculated using the outputs of the model simulations that will be discussed in Section 3.1. Figure 2b shows the radial distribution of l for the three groups. Our nominal SEF region is between $r = 80$ and 120 km for the data set. In these radii, the value of l ranges from 25 to 40 km. Therefore, we choose a 30 km radial smoothing that is, applied to the vorticity profiles shown in Figure 2 to illustrate pertinent vorticity features for the boundary layer updraft responses.

2.3. Axisymmetric and Asymmetric Forcing for the K18 Model

The pressure forcing at the K18 model top is represented by a single input of a two-dimensional nondivergent wind field, which can be either axisymmetric or asymmetric. For the three sets of azimuthal mean tangential wind composites discussed in Section 2.2, their corresponding two-dimensional axisymmetric realization is nondivergent by definition and therefore can be directly used as the forcing for the K18 model.

To utilize the capability of the K18 model to incorporate an asymmetric forcing, an asymmetric nondivergent wind field is required. This asymmetric nondivergent wind field was derived from the flight leg composites by the following procedure. First, to increase the likelihood that the derived wind asymmetries in the composites are organized by environmental wind shear, flight legs that have 850–200 hPa wind shear under $3 \mathrm{ms}^{-1}$ are removed. Here, the 850–200 hPa wind shear for each flight legs are extracted from the Statistical Hurricane Intensity Prediction Scheme database (DeMaria et al., 2005). Next, a running 90° azimuthal sector average is applied to the set of rescaled flight legs beginning at the shear vector pointing azimuth, and incrementing 45° steps, resulting in eight sector-averaged wind profiles. The purpose of this 90° averaging is two-fold. First, the sector averaging reduces the small-scale fluctuations in individual flight leg by incorporating information from multiple nearby flight legs. Second, this procedure assigns a relatively uniform weight to each flight leg despite their irregular azimuthal distribution.

These eight sector averages constitute an asymmetric tangential wind field that is, analyzed in two distinct ways. The first is by dividing the sectors into two quadrant sets. The first quadrant set (named Q1) is oriented such that the shear vector lies at the dividing line between two quadrants, namely Downshear-Left (DL), Upshear-Left (UL), Upshear-Right (UR), and Downshear-Right (DR). The second quadrant set (named Q2) is shifted 45° from the Q1 set, namely Downshear (DS), Left-of-Shear (LS), Upshear (US), and Right-of-shear

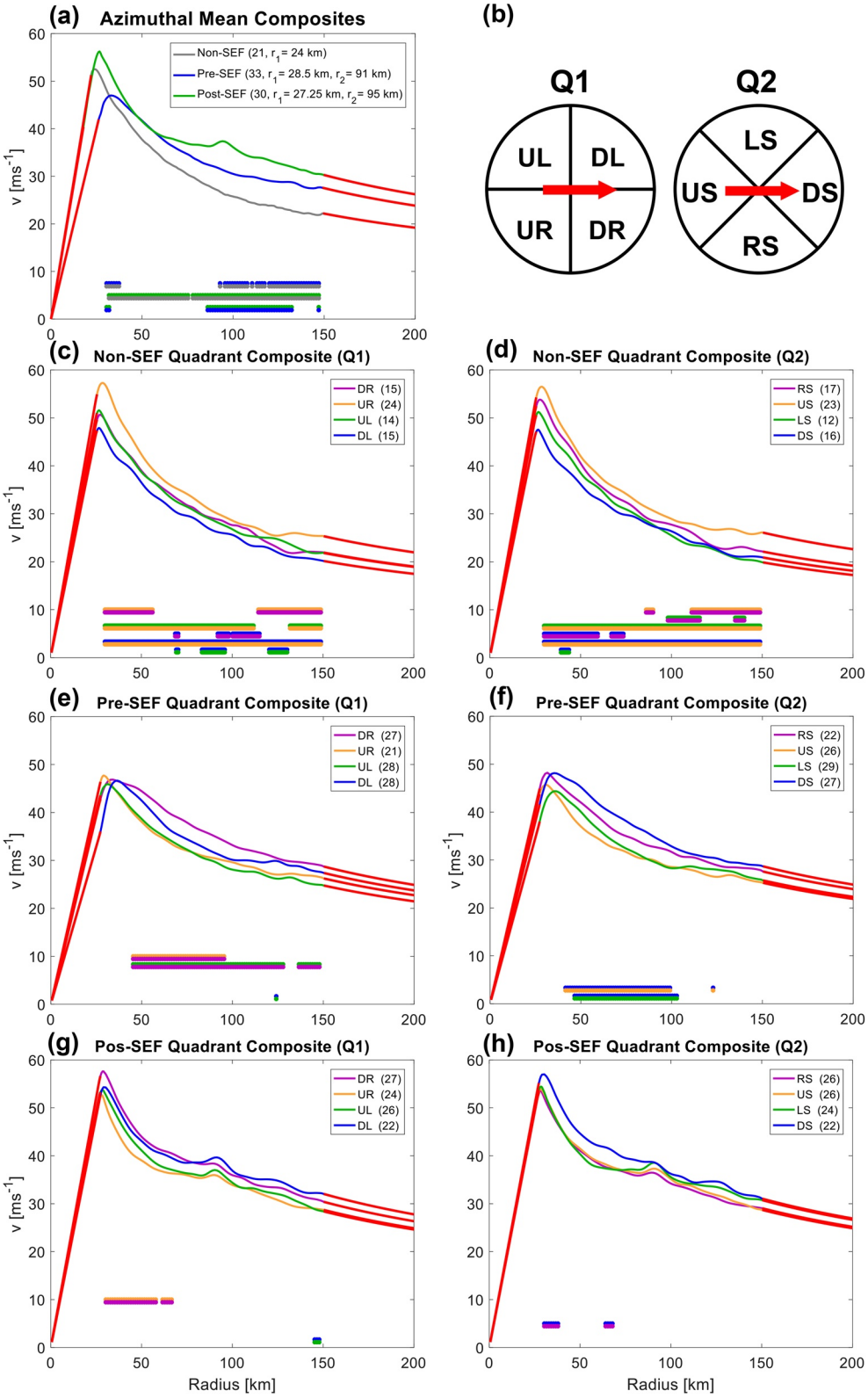
(a) Azimuthal Mean Composites
Non-SEF (21, r1 = 24 km)
Pre-SEF (33, r1 = 28.5 km, r2 = 91 km)
Post-SEF (30, r1 = 27.25 km, r2 = 95 km)
v [ms-1]
(b)
Q1
Q2
UL
DL
UR
DR
LS
US
DS
RS
(c) Non-SEF Quadrant Composite (Q1)
DR (15)
UR (24)
UL (14)
DL (15)
(d) Non-SEF Quadrant Composite (Q2)
RS (17)
US (23)
LS (12)
DS (16)
(e) Pre-SEF Quadrant Composite (Q1)
DR (27)
UR (21)
UL (28)
DL (28)
(f) Pre-SEF Quadrant Composite (Q2)
RS (22)
US (26)
LS (29)
DS (27)
(g) Pos-SEF Quadrant Composite (Q1)
DR (27)
UR (24)
UL (26)
DL (22)
(h) Pos-SEF Quadrant Composite (Q2)
RS (26)
US (26)
LS (24)
DS (22)
Radius [km]

Figure 1.

(RS). The orientations of these two sets of quadrants are shown in Figure 1b. The rescaled tangential wind and vorticity profiles of these two quadrant sets for each of the three SEF groups are shown in Figures 1c–1h and 2c–2h, along with locations of statistically significant differences. Similar to the azimuthal mean profiles, these sector-averaged profiles are used as individual axisymmetric forcing to drive the K18 model, as will be examined in Sections 3.2.2 and 3.3.

The second analysis approach derives a smoothed asymmetric nondivergent wind field from the eight sector averaged profiles, which is used as asymmetric forcing for the K18 model. This nondivergent wind field $\boldsymbol{v}_{\boldsymbol{\psi}}$ is expressed in terms of a stream function $\boldsymbol{\psi}$, that is, $\boldsymbol{v}_{\boldsymbol{\psi}} = \left(\partial\psi / \partial r, -1 / r\partial\psi / \partial\lambda\right)$. The stream function ψ is solved by applying the method of optimal interpolation to a low-pass filtered tangential wind field, which removes the signal of azimuthal wavenumbers greater than 4 (hereafter referred to as the filtered wind field v_o). It can be shown that the solution of the optimal interpolation is also the solution of the following generalized Poisson equation:

$$\frac{1}{r}\frac{\partial}{\partial r}\left(r\left(\frac{1}{\sigma_o^2}\right)\frac{\partial\psi}{\partial r}\right)+\frac{1}{r^2}\frac{\partial}{\partial\lambda}\left(\frac{1}{\sigma_B^2}\frac{\partial\psi}{\partial\lambda}\right)=\frac{1}{r}\frac{\partial}{\partial r}\left(r\left(\frac{v_o}{\sigma_o^2}\right)\right). \tag{1}$$

where (r,λ) are the polar coordinates, and σ_o^2 and σ_B^2 are the variances of observational and background uncertainties. The derivation of Equation 1, the solving procedure, and the method of determining the observational uncertainty σ_o^2 are discussed in the Appendix. Equation 1 is similar to the nondivergent component of the typical Helmholtz decomposition, but it further incorporates the information about the variance of observational uncertainty σ_o^2.

We show in Figure 3 the results for the Pre-SEF group as an example of our analysis technique. Figures 3a and 3b show the plan view of the filtered asymmetric tangential wind (v_o) and observational variance (σ_o^2). Multiple values of σ_B^2 have been tested, and it is found that the magnitude of σ_B^2 mainly affects the magnitude of u_ψ, but has little impact on ψ, v_ψ, and the simulated updraft response of the K18 model. For the results shown in Figure 1, the value of σ_B^2 is taken to be $1.93\,\mathrm{m^2 s^{-2}}$, which equals the azimuthal mean value of σ_o^2 at $r = 150$ km (highlighted by green circle in Figure 3b). From Figure 3a, we see that the tangential wind field in the downshear half of the storm is noticeably broader than the upshear half. This wind field broadening is in good agreement with WD18 and previous observational studies (e.g., Bell et al., 2012). As highlighted by the red contour, this expanded wind field almost appears as a secondary wind maximum. This structure of the tangential wind will be shown later as corresponding to a distinct band of local vorticity maximum that covers the entire DL and LS quadrants. Figures 3c and 3d show the tangential and radial components of the nondivergent wind $\boldsymbol{v}_{\boldsymbol{\psi}}$ for the Pre-SEF group after solving Equation 1. Overall, the tangential component of the nondivergent wind is more axisymmetric compared to the filtered asymmetric tangential wind (Figure 3a), but has a similar broadened signature in the LS quadrant. Note also that the radial component (Figure 3d) is about an order of magnitude smaller than the tangential component, and mostly concentrates at the primary eyewall.

3. Results

3.1. Axisymmetric Response

WD18 showed a clear axisymmetric broadening of tangential wind field in both the Pre- and Post-SEF groups, but not in the Non-SEF group. In this section, we first examine the K18 simulated axisymmetric boundary layer response using the azimuthal mean forcing of the three groups. As seen in Figure 4, the simulated boundary layers capture the fundamental structure of the TC boundary layer and compare qualitatively well with observations and full-physics simulations (Kepert & Nolan, 2014; F. Zhang et al., 2017; J. A.

Figure 1. (a) Azimuthal mean tangential wind composite profiles for Non-, Pre-, and Post-SEF groups. The sample count and median values of r_1 and r_2 are indicated in the legend. The portion of profiles highlighted in red indicate extrapolated region. (b) Schematics showing the orientations of the two sets of shear-relative quadrants, Q1 and Q2. (c) Quadrant averaged composite profiles for the Non-SEF group under Q1 quadrant definition (DL, UL, UR, and DR). (d) is the same as (c), but for the Q2 quadrant set of the Non-SEF group (DS, LS, US, and RS). (e and f) are the same as (c and d), but for the Pre-SEF group. (g and h) are the same as (c and d), but for the Post-SEF group. Statistically significant differences between each profile pair are plotted along the bottom of each plot with colors corresponding to each profile.

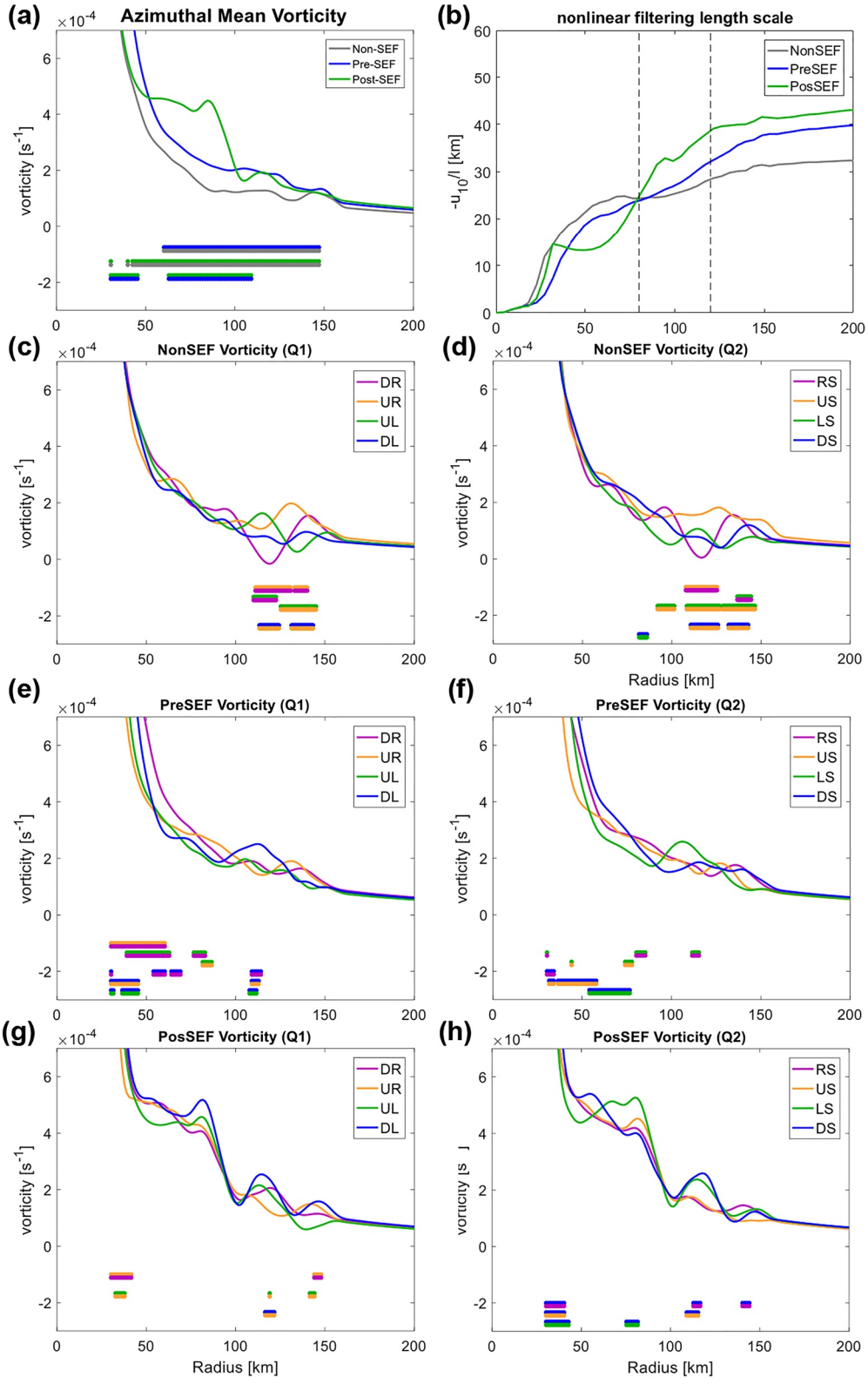
(a)
Azimuthal Mean Vorticity
Non-SEF
Pre-SEF
Post-SEF
vorticity [s-1]
(b)
nonlinear filtering length scale
NonSEF
PreSEF
PosSEF
-u10/f [km]
(c)
NonSEF Vorticity (Q1)
(d)
NonSEF Vorticity (Q2)
DR
UR
UL
DL
RS
US
LS
DS
(e)
PreSEF Vorticity (Q1)
(f)
PreSEF Vorticity (Q2)
(g)
PosSEF Vorticity (Q1)
(h)
PosSEF Vorticity (Q2)
Radius [km]

Figure 2.

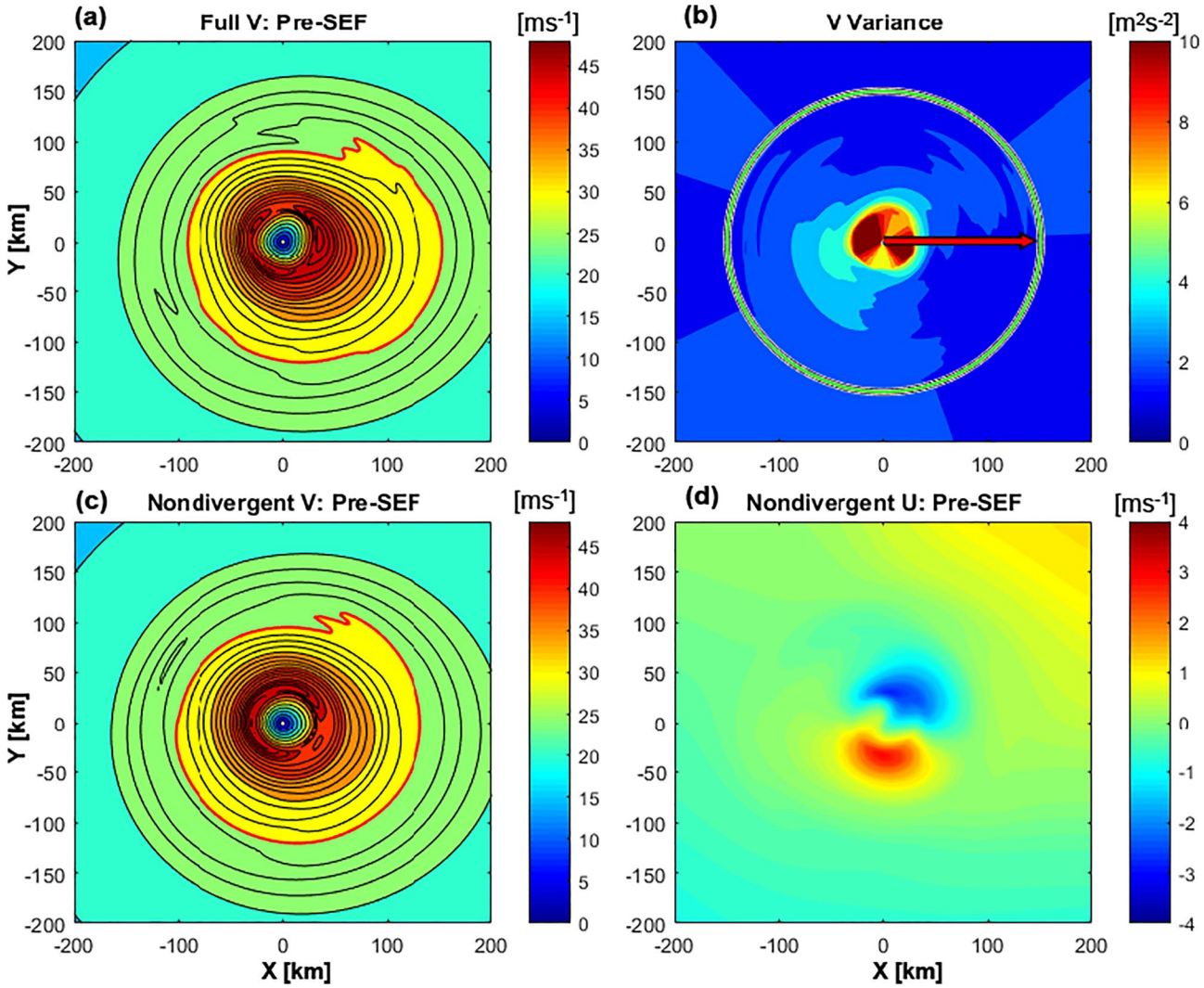

Figure 3. (a) The plan view of the filtered asymmetric tangential wind field v_o for the Pre-SEF group. The contour of 29.5 ms^{-1} is contoured in red to highlight the wind structure. The wind is contoured in black at every 0.5 ms^{-1} below 30 ms^{-1} and at every 1 ms^{-1} above 30 ms^{-1}. (b) The plan view of the observational variance obtained by the bootstrapping procedure for the Pre-SEF group. The green circle indicates 150 km radius. The red arrow indicates the environmental wind shear vector that defines the quadrant orientation. (c) The tangential component of the asymmetric nondivergent wind field $\boldsymbol{v}_{\psi}$ after solving Equation 2. Same contours are applied as in (a). (d) The radial component of the asymmetric nondivergent wind field $\boldsymbol{v}_{\psi}$.

Zhang et al., 2013). The boundary layer depth (as approximated by the height of 10% peak radial inflow) varies between 0.5 and 1 km outside the eyewall and out to 200 km radius. These depths are slightly lower than those found in the observations-based axisymmetric composites from J. A. Zhang et al. (2011), but these are still realistic depths that fall within the range of observed boundary layer depths (Kepert et al., 2016; J. A. Zhang et al., 2013). While discrepancies between our simulated depths and boundary layer depths in other studies may occur, these do not impact our conclusions which are based on the emergence and location of

Figure 2. (a) Azimuthal mean vorticity composite profiles for Non-, Pre-, and Post-SEF groups. (b) Radial profile of the nonlinear filtering length scale $l = -u_{10} / I$ for Non-, Pre-, and Post-SEF groups, computed from the axisymmetric K18 model simulations for the three groups. Vertical dashed lines highlight the 80 and 120 km radii. (c) Quadrant averaged vorticity composite profiles for the Non-SEF group under Q1 quadrant definition (DL, UL, UR, and DR). (d) is the same as (c), but for the Q2 quadrant set of the Non-SEF group (DS, LS, US, and RS). (e and f) are the same as (c and d), but for the Pre-SEF group. (g and h) are the same as (c and d), but for the Post-SEF group. Statistically significant differences between each profile pair are plotted along the bottom of each plot with colors corresponding to each profile.

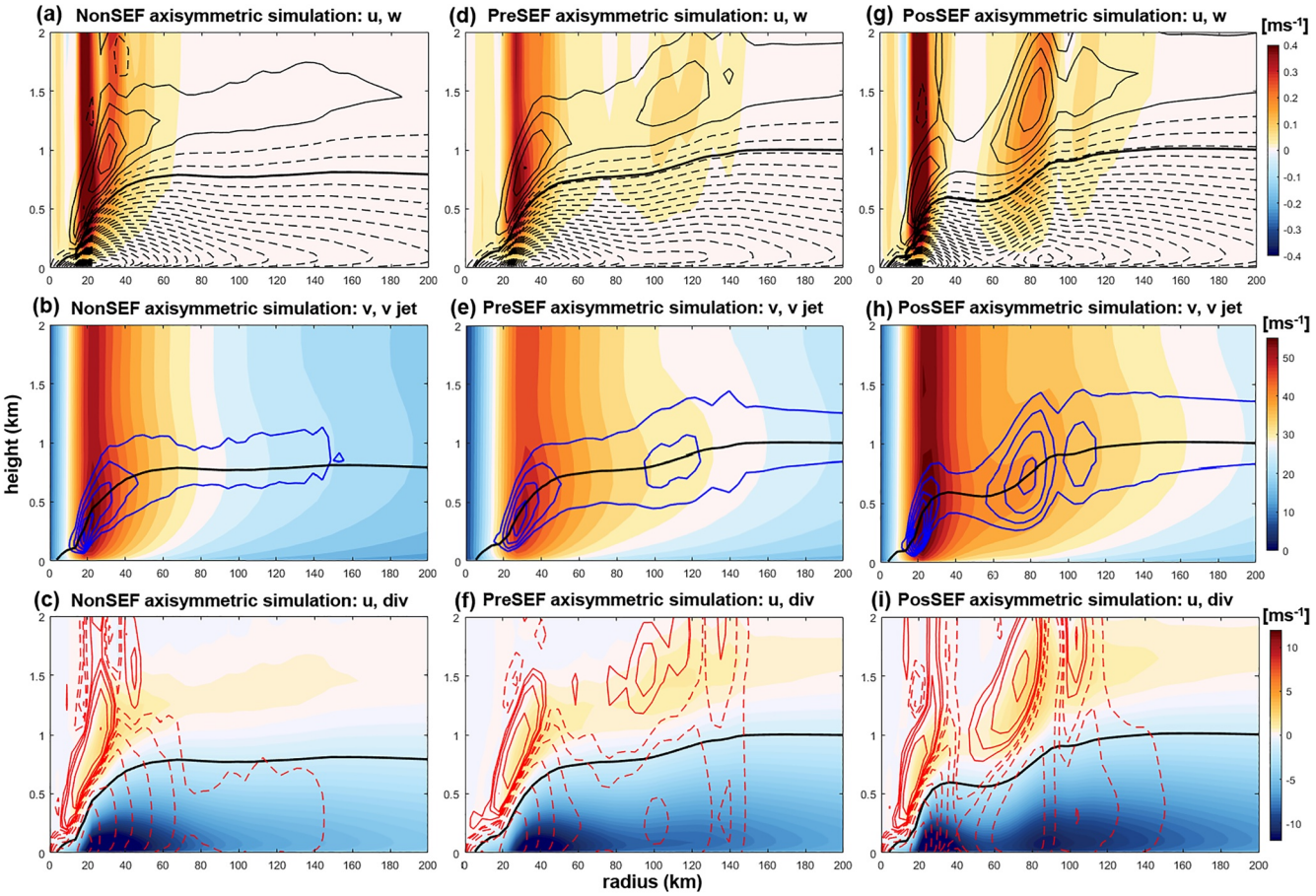

Figure 4. Boundary layer axisymmetric simulation responses using the Non-SEF (left column), Pre-SEF (middle column), and Post-SEF (right column) azimuthal mean profiles (Figure 1a). The top row (a, d, and g) displays vertical velocity (shaded) and radial velocity (black contours; dashed for inflow and solid for outflow), with radial velocity contoured every 0.8 ms^{-1} and the zero-line omitted. The middle row (b, e, and h) displays tangential wind v (shaded) and positive gradient wind (contours), contoured at every 0.6 ms^{-1} with zero-line omitted. The bottom row (c, f, and i) displays radial velocity (shaded) and horizontal divergence (red contours; dashed for convergence and solid for divergence), contoured at $(\pm 2, \pm 4, \pm 8, \pm 16, \pm 32, \pm 64, \pm 128, \pm 256) \times 10^{-5} s^{-1}$. The thick black solid contour shows the 10% contour level of the maximum inflow.

updraft responses; this is because the updrafts in our model are not sensitive to the simulated depth, but rather the gradient wind structure aloft.

Figures 4a–4c show the boundary layer response of the Non-SEF group simulated by the K18 model. The updraft maximum of the primary eyewall lies near the radius of 20 km, which is consistent with the RMW of the Non-SEF group shown in Figure 1a. Figure 4b shows the boundary layer tangential wind. The positive gradient wind, calculated as the difference between the actual tangential wind and the gradient wind, is shown by the blue contours. This field reveals the tangential wind jet of the primary eyewall, which is supergradient in nature (KW01; Kepert, 2013). The associated inflow maximum lies beneath and just slightly outward (near $r = 30$ km) from the updraft maximum, as shown in Figure 4c. As expected, no secondary eyewall signature is found outside of the primary eyewall. The updraft, supergradient wind, and horizontal convergence maxima of the primary eyewall are the dominant features from each field.

Figures 4d–4f show the boundary layer response of the Pre-SEF group. Similar to the Non-SEF group (Figure 4a), in Figure 4d we see the updraft maximum of the primary eyewall near the $r = 27$ km, which is consistent with the RMW of the forcing profile (r_1 in Figure 1a). Outside the primary eyewall, substantial upward motion can be seen covering 80–140 km radii, with a secondary updraft maximum near 100 km radii, roughly consistent with the r_2 value shown in Figure 1a. Associated with this secondary updraft maximum

is a local outflow maximum at the same level. This overturning circulation is a preceding signature of the incipient secondary eyewall.

Figure 4e shows the tangential wind structure within the boundary layer. Compared to the Non-SEF group (Figure 4b), this boundary layer tangential wind field is more broadened, and contains a secondary supergradient tangential jet (blue contour in Figure 4e). Figure 4f shows the radial flow and divergence within the boundary layer. Within the inflow layer, enhanced horizontal convergence occurs at 100 km due to a slight local weakening of the boundary layer inflow nearby. This airflow then turns into the updraft seen in Figure 4d. Overall, the existence of secondary maxima of boundary layer updraft, tangential wind jet, and convergence signals the existence of an incipient secondary eyewall in the Pre-SEF group, which is not seen in the Non-SEF group. These outer eyewall flow features are similar to those found in previous studies using a similar model, as in Kepert (2013) and Kepert and Nolan (2014), and K18, but are here shown using observational data.

Figures 4g–4i show the boundary layer response of the Post-SEF group. Compared to the Pre-SEF group, the overall signatures of the now-developed secondary eyewall are significantly stronger. As shown by the vertical velocity in Figure 4g, the secondary eyewall updraft is now located between $r = 80$ and 90 km, signaling a clear inward contraction compared to the Pre-SEF group. This inward contraction is associated with the inward shift of the outer vorticity anomaly between the Pre-SEF and Post-SEF groups (Figure 2a). Such inward contraction is expected once the secondary eyewall is well established, which acts as an axisymmetric heat source within a vortex (Shapiro & Willoughby, 1982). The secondary updraft maximum also becomes noticeably stronger and deeper. In the radial wind (Figure 4i), a secondary inflow maximum emerges with a magnitude similar to that of the primary eyewall. This associated convergence maximum is located just radially inward of the secondary updraft, which is also stronger and occupies a broader radial range compared to the Pre-SEF group. Compared to the Pre-SEF group, the Post-SEF tangential winds (Figure 4h) of the secondary eyewall are strengthened significantly, and almost appear as an isolated tangential wind maximum. The calculated tangential jet of the secondary eyewall is also more substantial.

3.2. Asymmetric Response

Even though the azimuthal mean profile of the Pre-SEF does not have a clear secondary wind maximum (Figure 1a), the forcing profile was sufficient to force a clear but weak secondary maximum of inflow, updraft, and supergradient tangential wind jet within the boundary layer (Figures 4d–4f). We now seek evidence to determine if there is a specific azimuthal region that contributes more to this incipient secondary eyewall signal by using the K18 model in conjunction with the asymmetric nondivergent wind field of the Pre-SEF group, as shown in Figures 3c and 3d. The results can provide insight into which quadrant possesses the earliest asymmetric features that can induce boundary layer responses favorable to the subsequent SEF process.

3.2.1. Asymmetric Simulation of the Pre-SEF Group

Figure 5 summarizes the results of the asymmetric response simulated by the K18 model using the 2-dimensional asymmetric forcing (from Figures 3c and 3d). Figure 5a shows the azimuthal average of the response. Comparing this to Figure 4, the azimuthal mean response based on the 2D asymmetric forcing is in nice agreement with the axisymmetric response simulated using the azimuthal mean forcing (Figures 4d–4f). The radial location, structure, and magnitude of the azimuthal mean secondary updraft and radial outflow maxima are consistent with the axisymmetric forcing simulation, despite the fact that the nonlinear K18 simulation is driven by asymmetric vorticity forcing (Figure 5b).

Figure 5c shows the plan view of the updraft response near 1 km altitude. The shear direction that defines the quadrant orientation is illustrated by the red arrows. From Figure 5c, we see that the azimuthal mean updraft at the secondary eyewall location mostly comes from the left-of-shear half of the storm (DL, LS, and UL quadrants). Here, a distinct updraft band begins in the downshear direction, strengthens downwind, and maximizes in the LS quadrant of the storm. This updraft band also coincides both radially and azimuthally with a distinct vorticity band in the forcing field (Figure 5b). This collocation of the updraft response and vorticity forcing is consistent with the theoretical analysis presented in Kepert (2001 and 2013), which showed that in the steady-state limit the updraft response is directly linked to the vorticity forcing aloft.

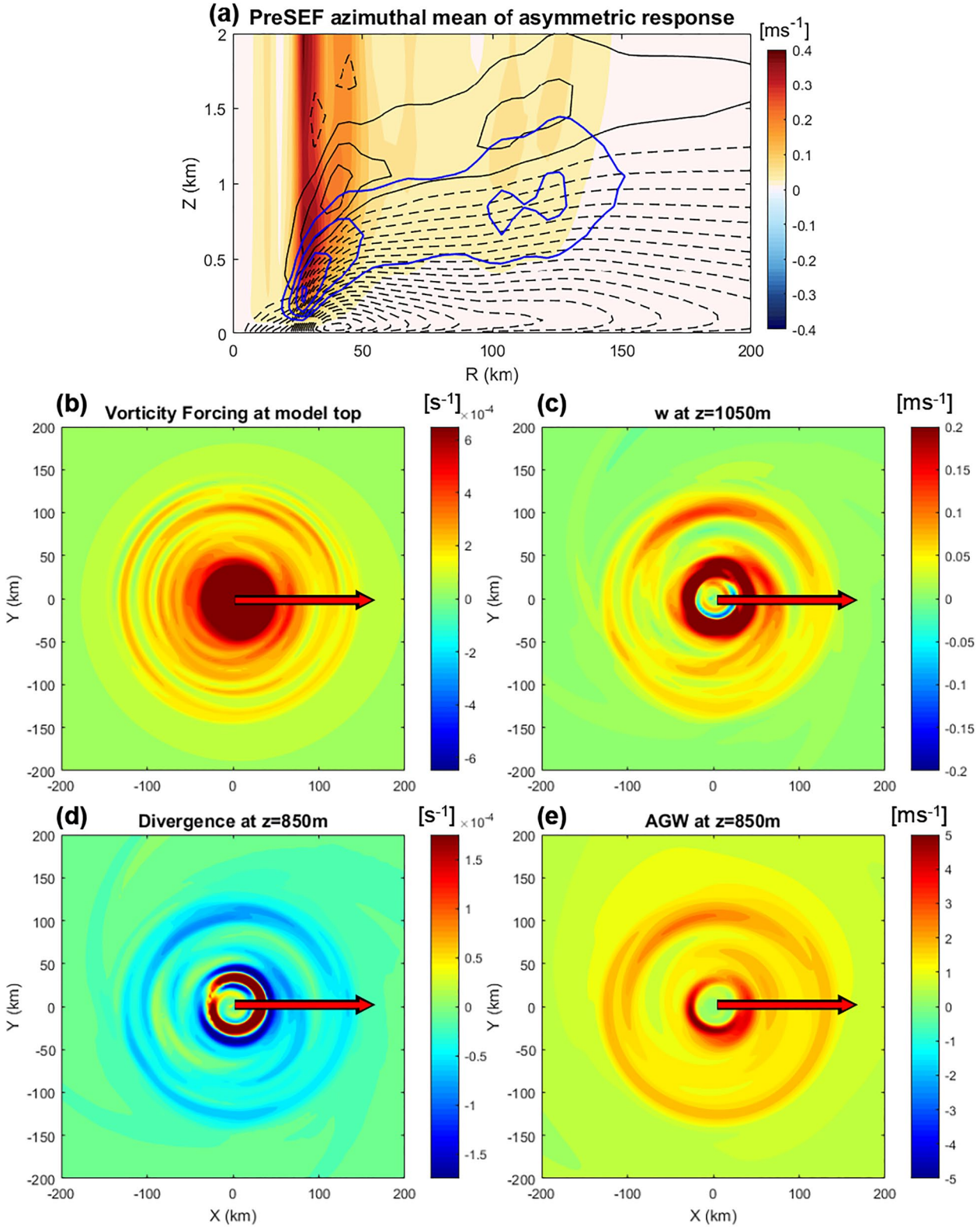

Figure 5. (a) Azimuthal mean of the boundary layer asymmetric simulation response using the Pre-SEF forcing (forcing field shown in Figure 3c). Shown are the azimuthal mean vertical velocity (shading), supergradient wind (blue contours, at every 0.8 ms^{-1}), and radial velocity (black contours, at every 0.6 ms^{-1} with 0 line omitted). (b) The plan view of the vorticity forcing at the model top. (c–e) same as (b), but for vertical velocity response at $z = 1.05$ km; divergence forcing at $z = 0.85$ km; and gradient wind at $z = 0.85$ km. The red arrows illustrate the environmental shear vector.

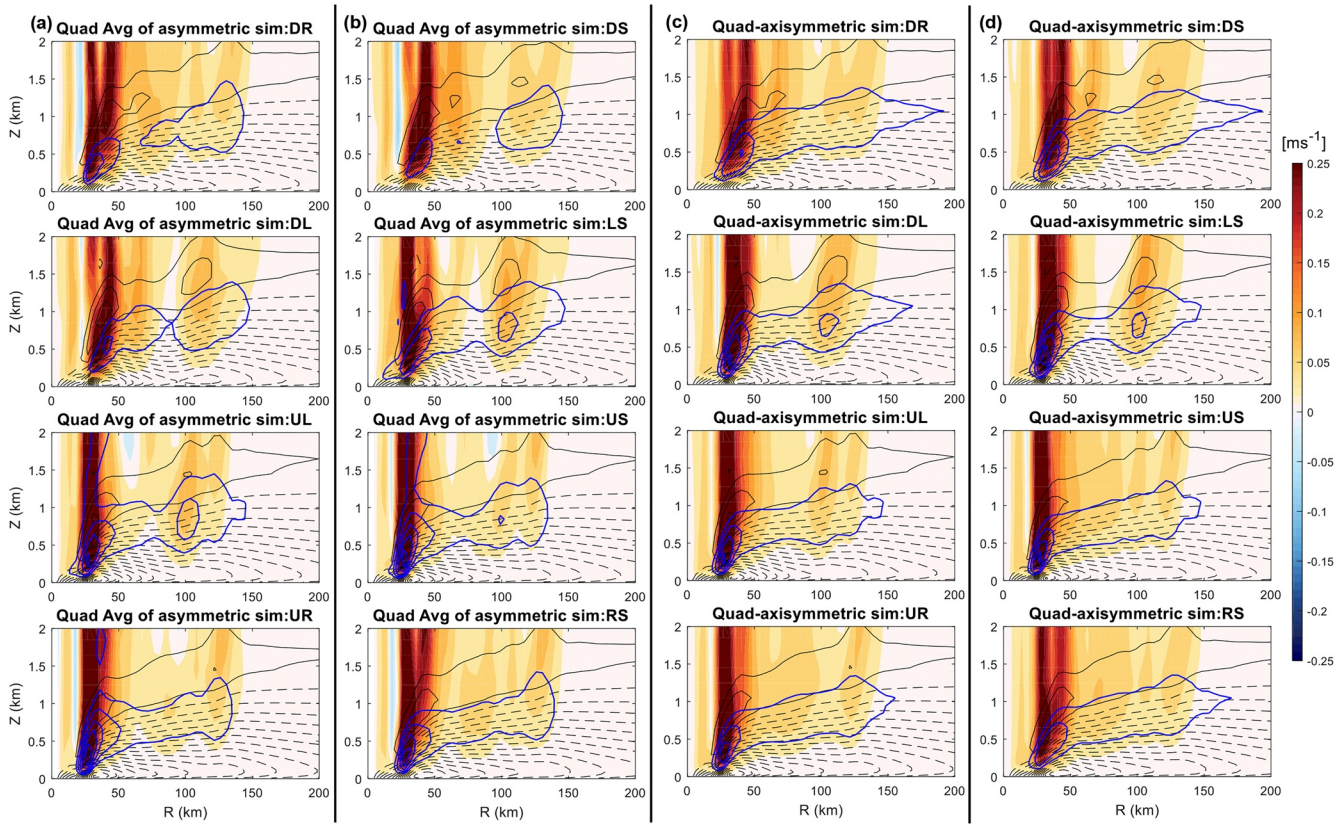

Figure 6. (a and b) Quadrant averages of the asymmetric simulation responses using the Pre-SEF forcing (forcing field shown in Figure 3c). Shown are the mean vertical velocity (shading), supergradient wind (blue contours, at every 1 ms^{-1}), and radial velocity (black contours, at every 0.8 ms^{-1} with 0 line omitted). Quadrant averages are taken for the (a) Q1 and (b) Q2 quadrant sets. (c and d) as in are the same as (a and b), but for axisymmetric simulation responses that use forcing from quadrant averages of the Pre-SEF forcing field. These experiments are called "quadrant-axisymmetric" simulations.

Figures 5d and 5e show the plan view of convergence and gradient wind at $z = 850$ m, which is just underneath the updraft shown in Figure 5c. The convergence field follows the pattern of the updraft response, which is expected from the continuity equation. However, it is also interesting to note that compared to the enhanced updraft and convergence regions, the strongest supergradient wind displays a noticeable downwind shift toward the upshear quadrants.

3.2.2. Quadrant-Averaged Analysis of the Pre-SEF Group

Figures 6a and 6b show the quadrant-averaged cross-sections of vertical motion and radial velocity across the Q1 and Q2 quadrant sets. Consistent with the plan view of the updraft response (Figure 5c), the quadrant-averaged structures show that secondary updraft maxima can be found in all the quadrants, but the outer updraft maxima in the DL and LS quadrants are noticeably enhanced. In the DL quadrant, a clear secondary inflow maximum underneath the outer updraft appears. Traveling downwind, the updraft and inflow maxima reach their strongest intensity in the LS quadrant. Further downwind, these secondary eyewall signals start to weaken, as seen in the UL and US quadrants. The secondary updraft and inflow maxima in the DL, LS, and UL are noticeably stronger than both the azimuthal means of the asymmetric (Figure 5a) and the axisymmetric simulations (Figure 4d). These greater magnitudes indicate that the incipient axisymmetric secondary eyewall signal found in Figures 5a and 4d indeed comes largely from the left-of-shear quadrants.

Meanwhile, both the supergradient wind and radial outflow maxima exhibit a noticeable downwind shift compared to the azimuthal locations of the updraft and boundary layer inflow maxima. The supergradient wind is strong in the LS quadrant (second panel of Figure 6b) and becomes strongest in the UL quadrant (third panel of Figure 6a), while strong updrafts begin more upwind in DL, and maximize in the LS

quadrant. Furthermore, the downwind shift in the outflow is even more apparent. For instance, the strong outflow actually begins in the LS, and then becomes strongest in the UL and US quadrants. This shift is consistent with the tangential wind jet and supergradient outflow as occurring after and as a result of the enhanced inflow and updraft (Kepert, 2001, 2013).

We have so far examined quadrant averages of the asymmetric simulation response using the 2D asymmetric forcing. Following the analyses of K18, we now will compare these results to *axisymmetric* simulation responses using *quadrant averages* of the 2D forcing field; we will call these experiments "quadrant-axisymmetric" simulations as opposed to the earlier quadrant averages of the asymmetric simulations. We first compute the quadrant averages of the nondivergent tangential wind (as in Figure 3c), which are then used as to force the axisymmetric K18 simulations. Figures 6c and 6d show these quadrant-axisymmetric simulation responses for each quadrant. The quadrant-axisymmetric responses are able to capture the radial location and magnitude of the secondary updraft and inflow maxima, as seen in Figures 6a and 6b. This is particularly clear for the DL, LS, and UL quadrants (second panels of Figures 6c and 6d and third panel of Figure 6c) where the outer updraft is strong. Associated with these outer updrafts, the vorticity profiles for the DL and LS quadrants also show local maxima near $r = 100$ km (Figures 2e and 2f), where the DL maximum is also statistically significant compared to the other Q1 quadrants. Differences in the updraft response can be found in the US quadrant, where the quadrant-axisymmetric simulation (third panel of Figure 6d) has some weak, intermittent updrafts in the moat region between 60 and 80 km radius, while these intermittent updrafts appear to be weaker in the asymmetric simulation (third panel of Figure 6b). This indicates that the distinct outer updraft signal in the US quadrant of the asymmetric simulation may be due to the downwind influence from the upwind quadrants (DL, LS, and UL). The generally good agreement in the updraft responses between Figures 6a and 6b and Figures 6c and 6d indicates that the outer vorticity forcing at the DL and LS quadrants exert significant influence on the quadrant-averaged updraft and inflow in the local and downwind quadrants.

By comparing the supergradient wind and radial outflow between Figures 6c and 6d and Figures 6a and 6b, we see that the downwind shift signature of the supergradient wind and outflow is not present in the quadrant-axisymmetric simulation responses. In the quadrant-axisymmetric simulation (Figures 6c and 6d), strong supergradient wind and radial outflow maxima are only seen in the DL and LS quadrant, while in the asymmetric simulation the strongest outer maxima of supergradient wind and radial outflow clearly shift further downwind and extend into the upshear quadrants (UL and US). This suggests that the downwind shift in the supergradient wind and outflow in the steady-state response is the consequence of the azimuthal advection acting upon the asymmetric flow induced by the localized asymmetric forcing (consistent with K18), and that the supergradient wind and outflow are dynamically connected (as consistent with Kuo [1971], KW01, Abarca and Montgomery [2013]).

3.2.3. Quadrant-Averaged Analysis of the Non-SEF and Post-SEF Groups

As for the Non-SEF and Post-SEF groups, it is found that the Post-SEF boundary layer response is dominated by the axisymmetric component, while the Non-SEF response at the outer core region is generally weaker. Given the results in our previous section that the axisymmetric simulation response using quadrant-averaged forcing (the quadrant-axisymmetric simulation) is a good approximation for the quadrant-averaged response of the asymmetric simulation, for simplicity, we only present the result of the quadrant-axisymmetric simulations.

Figure 7 shows the comparison of the responses using the quadrant-averaged wind profiles as forcing for the Non-SEF (Figures 1c and 1d) and Post-SEF groups (Figures 1g and 1h). For the Post-SEF group, as shown in Figures 7a and 7b, the boundary layer response displays clear secondary maxima of updraft, inflow, and supergradient outflow across all eight overlapping quadrants. Comparing the strength of these signals, it is found that the strongest secondary eyewall signature lies in the DL, LS, UL, and US quadrants. These left-of-shear dominant signatures are consistent with that of the Pre-SEF signatures, but stronger and extending further downwind into the US quadrants.

Looking into the Non-SEF response (Figures 7c and 7d), we note that while most quadrants only have a signal at the primary eyewall, noticeable outer updrafts are found in the US and UR quadrants. As shown in Figures 1c, 1d, 2c and 2d, the quadrant-averaged profiles for these two quadrants do exhibit discernible

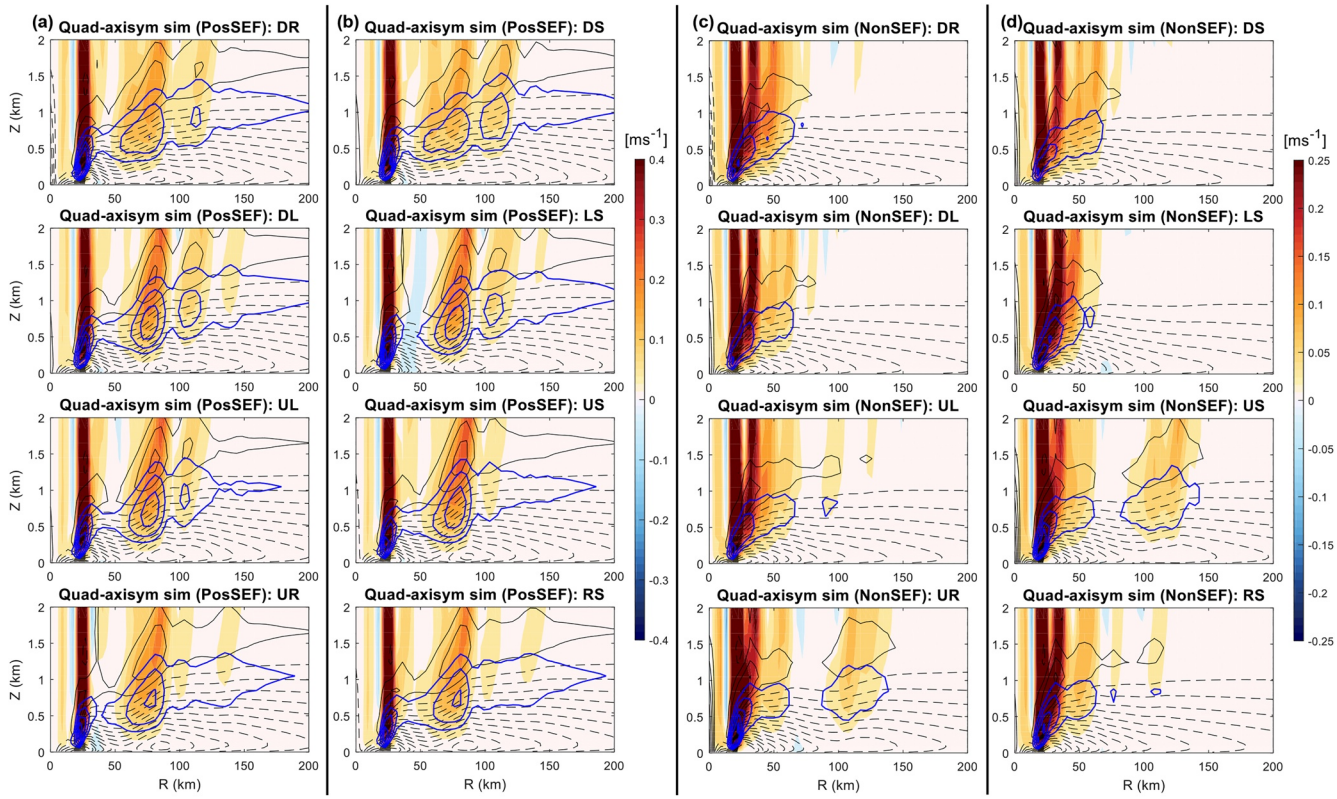

Figure 7. Quadrant-axisymmetric simulation responses using forcing from quadrant-averaged profiles of the (a and b) Post-SEF and (c and d) Non-SEF groups (forcing profiles shown in Figure 1). Shown are the vertical velocity (shading), radial inflow (contoured in black at every 1 ms^{-1} with 0 line omitted), and supergradient wind (contoured in blue, at every 1 ms^{-1}). Quadrant-averaged profiles are taken throughout the Q1 (a and c) and Q2 (b and d) quadrant sets.

wind field broadening, where the associated vorticity anomalies induce local updraft responses in these quadrants. However, these responses are weaker than that in the Pre-SEF responses (Figures 6c and 6d), and are only isolated within these two quadrants. Thus, these signals are not able to project strongly onto the azimuthal mean (Figure 4a), unlike for the Pre-SEF group.

3.3. Sensitivity Analysis of Updraft Variability

The results from the previous section demonstrated that the early secondary eyewall signature present in the azimuthal mean response of the Pre-SEF group largely comes from an outer band of updraft maximum located in the left-of-shear half of the storm, which persists and further extend to the upshear quadrants in the Post-SEF group. This updraft band is dynamically tied to the vorticity maximum near the same region. In order to further examine the robustness of the updrafts in this region, this section explores the sensitivity of the updraft signature to variability in forcing structures across different storm quadrants.

3.3.1. Bootstrapping Analysis of the Outer Updraft Strength

This variability analysis uses the bootstrapping method and subset samples that determined the tangential wind variance field (Figure 3b). For each of the overlapping quadrants, 30 representative sets of bootstrap samples are selected based on specific criteria. In each bootstrap sample, any member can only repeat at most one time, and exactly a quarter of the members are repeated. The requirement on the maximum number of reoccurrences of the members is to avoid over-emphasizing the forcing profiles of any particular member, and the requirement of having a quarter of members being repeated is to ensure that the set of selected bootstrap samples in each quadrant are subject to the same degree of variability. Next, the average of each bootstrap sample set is computed, which is then used as an axisymmetric forcing for the K18 model. We use axisymmetric forcing for each quadrant (the quadrant-axisymmetric simulations) since, as shown

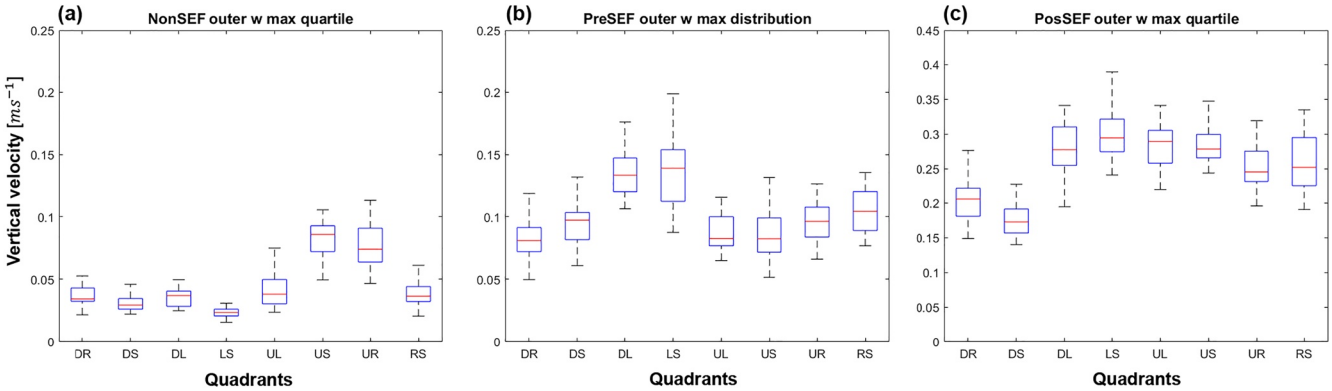

Figure 8. Box plots (showing the 25th, 50th, and 75th percentiles) of the outer maximum updraft distributions for the Q1 and Q2 quadrants for (a) the Non-SEF group; (b) the Pre-SEF group and (c) the Post-SEF group. The outer maximum updraft is defined as the maximum updraft in between 90 and 140 km radii. Note that the ranges of vertical velocity for (a and b) are up to 0.25 ms^{-1}, but for (c) is up to 0.45 ms^{-1}.

in Figure 6, its updraft response closely approximates that of the quadrant-averaged response to asymmetric forcing. In total, the K18 model is run with 240 sample sets (30 per quadrant) for each of the three SEF groups.

Figure 8 summarizes the results of the sensitivity experiments by showing the quartiles and the extreme values of the maximum outer updraft in all quadrants of the three groups. Here, the maximum outer updraft is defined as the maximum value of the vertical velocity between 90 and 140 km radial range. For the Non-SEF group (Figure 8a), the bootstrapping result shows that only the US and UR quadrants show higher medium values of the outer updrafts, while the other quadrants have medium updraft values less than 0.05 ms^{-1}. This verifies the findings of Figures 7c and 7d that the outer updrafts in the US and UR quadrants are weak and isolated, and therefore not sufficient to project strongly into the azimuthal mean.

Figure 8b shows the bootstrapping results for the Pre-SEF group, which is distinct contrast compared to the Non-SEF. Not only the outer updrafts generally become stronger in most quadrants, the updraft strength in the DL and LS quadrants are noticeably higher. Specifically, the median updraft strength of DL (0.1337 ms^{-1}) and LS (0.1393 ms^{-1}) are both as strong as that of the strongest member of the other quadrants (0.1357 ms^{-1} in RS). Furthermore, the 25th percentiles of DL and LS are both higher than the 75th percentiles of most of the other quadrants. This result shows that the outer updraft signals in the DL and LS quadrants are noticeably stronger than the other quadrants, and that these left-of-shear signals are robust features that emerge before other regions leading into SEF.

Moving on to the Post-SEF group (Figure 8c), consistent with the quadrant average structure shown in Figures 7a and 7b, the outer updraft distributions in Post-SEF becomes substantially stronger across the eight quadrants across the eight quadrants, with a smaller medium value of 0.175 ms^{-1} lying at the DS quadrant. Starting from DL and cyclonically downwind, the outer updraft maximum is noticeably stronger, with the 25 percentiles of the DL, LS, UL, and US quadrants greater than the 75 percentiles of the DS and DR quadrants. This verifies the findings in Section 3.2.3 that the left-of-shear enhancement of the outer updraft in the Pre-SEF is a robust signal that persists and extends further cyclonically downwind in the Post-SEF group.

3.3.2. Variability of the Boundary Layer Response in Pre-SEF Ensemble

Bootstrapping results in Section 3.3.1 show that the outer updraft in the DL and LS quadrants of Pre-SEF groups is noticeably stronger than the other quadrants, which persists into the Post-SEF groups and extends further downwind. To further examine the structural variability of these signals, in this section we examine the differences in the boundary layer structure across the bootstrapping ensemble members of the Pre-SEF group.

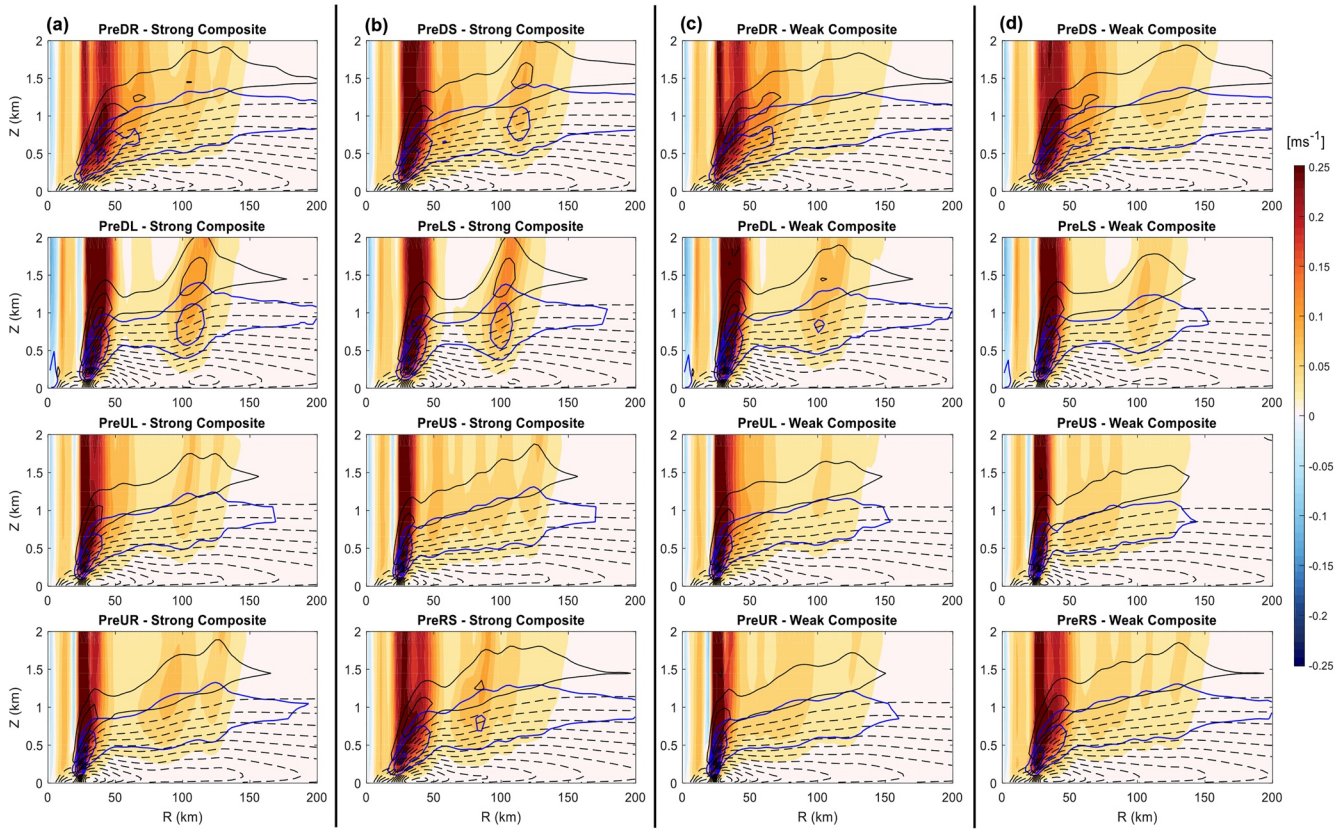

Figure 9. (a) Composites of the simulation responses using the 8 Pre-SEF members with the strongest outer updrafts in the Q1 quadrant set. Shown are the composite of the vertical velocity (shading), radial inflow (contoured in black at every 1 ms^{-1} with 0 line omitted), and supergradient wind (contoured in blue, at every 1 ms^{-1}). (b) Same as (a), but for the strong composite of the Q2 quadrant set. Panels (c and d) are the same as (a and b), but for the weak composites of the Q1 and Q2 quadrant sets of the Pre-SEF group.

Figure 9 shows the cross-section composites of the strongest and weakest eight members of the 30 bootstrap samples in each of the quadrants of the Pre-SEF group (herein referred as the strong and weak composites, respectively). Consistent with the previous results, in the strong composites (Figures 9a and 9b) both the DL and LS quadrants have a clean distinct outer updraft maximum and a clear moat region. The outer inflow and supergradient maxima are also distinct. In the quadrants downwind, just as with the full sample response (Figure 6), the outer updraft maxima become noticeably weaker (US) with a less clear moat that has weak intermittent updrafts. The radial inflow and supergradient wind also do not have a clear isolated maximum at these quadrants.

Similarly, for the weak composites (Figures 9c and 9d), the secondary updraft maxima in the DL and LS quadrants are still clear and are noticeably stronger than that of the other quadrants. The moat remains well-defined with no clear intermittent updrafts. The result herein shows that the isolated outer maxima of updraft and radial inflow in the DL and LS quadrants are robust features that exist cross both the strongest and weakest subsets of the bootstrap samples. In contrast, the signals in most other quadrants are less consistent in comparison. For instance, the isolated outer updraft maximum in the strong composite of UR is found absent in the weak composite, indicating that the signal seen in strong composite could be due to a small subset of flight legs not included in the weak composite. The findings here suggest that the DL and the LS quadrants in the Pre-SEF group possess the earliest robust signature of an emerging secondary eyewall.

4. Discussion and Conclusions

In this study, we examined the TC boundary layer response to imposed free-tropospheric forcing derived from observations to investigate the axisymmetric and asymmetric boundary layer response during SEF. Observed tangential wind composite profiles of storms without SEF, prior to SEF, and after SEF (Non-, Pre-, and Post-SEF; Wunsch & Didlake, 2018) are used to the force the Kepert (2018) diagnostic boundary layer model (the K18 model), which is integrated for 48 h to examine the steady-state boundary layer response to the tropospheric forcing.

The axisymmetric Post-SEF composite observation profile exhibited the expected secondary wind maximum of the secondary eyewall, and the simulated boundary layer response to this profile showed the canonical structure of an existing secondary eyewall, with strong maxima of updraft, boundary layer inflow, and convergence. Although the axisymmetric Pre-SEF composite profile did not have a noticeable secondary wind maximum, this profile exhibited a notably broadened wind field compared to the Non-SEF composite, and that the vorticity structure was sufficient to induce a clear simulated boundary layer response associated with the incipient secondary eyewall. In contrast, the Non-SEF profile did not induce any notable response outside of the primary eyewall.

We next derived an asymmetric nondivergent wind field from the Pre-SEF composite and then used it to drive the K18 model. This asymmetric wind field displayed a broadened tangential wind field and an enhanced vorticity band in the downshear and left-of-shear regions. The simulated boundary layer response had a clear band of outer updraft and strengthened boundary layer inflow, corresponding to the vorticity band in the asymmetric wind field, primarily in the left-of-shear quadrants. When applying the model with quadrant-averaged forcing, our goal was to determine which quadrants possess early signals of wind structures that can best support and accompany a burgeoning secondary eyewall updraft and circulation. Our results indicate that the strongest signal is indeed in the DL and LS quadrants of the Pre-SEF group, which is driven largely by the vorticity structure of the broadened tangential wind field in these quadrants. Applying the quadrant-averaged analysis to the other two groups, our results indicate that the K18 model correctly produces no organized secondary updraft in most quadrants of the Non-SEF groups, while also diagnosing clear secondary eyewall updraft in all quadrants of the Post-SEF composites.

It is also confirmed via bootstrapping analyses that the enhanced updrafts in the DL and LS quadrants of Pre-SEF group are a more robust signal than that of the other quadrants, with a clear moat and secondary updraft maximum exist in both the strong and weak member composites. The Post-SEF bootstrapping experiment shows that the already-formed secondary eyewall exhibits the strongest updraft in the DL and LS quadrants and extends cyclonically downwind into the upshear quadrants. The bootstrapping analysis for the Non-SEF group, on the other hand, shows that the outer updraft signals in non-SEF period are weaker and more localized azimuthally, and thus fail to project onto the azimuthal mean.

The findings discussed above suggest an important dynamical connection between the expanded wind and vorticity fields in the left-of-shear quadrants and the subsequent occurrence of the SEF process, and that these left-of-shear enhancements are an unambiguous and repeatable signal of ongoing SEF processes in these composite observed cases. This is an intriguing result because in observed and simulated sheared TCs, the outer regions are often populated by a shear-organized rainband complex, with its convectively active portion lying to the right of the wind shear vector and broad stratiform precipitation in the left-of-shear quadrants (Hence & Houze, 2012a, 2012b; Li et al., 2017; Willoughby et al., 1984). Within the left-of-shear stratiform rainband, a MDI feature has been frequently identified in observations (Didlake & Houze, 2013; Didlake et al., 2017, 2018) and has been largely attributed to latent cooling in the stratiform regions (Chen, 2018; Chen et al., 2018; Dai et al., 2017; Qiu & Tan, 2013; Tyner et al., 2018; Yu & Didlake, 2019; Zhu et al., 2015). Yu et al. (2021) showed that the MDI in the left-of-shear stratiform precipitation region was accompanied by inward advection of angular momentum, which preceded the emergence of a sustained low-level updraft in the left-of-shear regions. It is possible that MDIs are present in some form in our composite storms, and led to the observed asymmetric storm-scale broadening of the tangential wind above the boundary layer. The left-of-shear wind field expansion may not be *necessary* for SEF to occur, but it is at least critical for this particular sequence of pre-SEF processes in sheared TCs—a sequence that emphasizes outer

rainbands accelerating the left-of-shear tangential wind field and reinvigorating low-level updrafts through interactions with the boundary layer.

While our results here suggest the importance of left-of-shear processes prior to the onset of SEF, the composite mean of the tangential wind observations can only reveal the general features that commonly exist in the storm samples. Uncertainty remains in determining what exact processes are responsible for these asymmetric features in these quadrants. In addition, the exact mechanisms that led to the observed SEF in our data set still require further investigation. It remains possible that VRWs in the left-of-shear quadrants led to acceleration of the left-of-shear tangential winds and thus enhanced local vorticity, as described by Guimond et al. (2020). The resulting VRW-induced left-of-shear vorticity enhancement would induce a boundary layer response like that seen in the current results. It also remains possible that VRWs led to a direct spin-up of the axisymmetric secondary tangential wind maximum in our SEF cases (Fischer et al., 2020; Guimond et al., 2020; Montgomery & Kallenbach, 1997). Distinct from direct spin-up mechanisms, the axisymmetrization of the observed left-of-shear features also remains a possible factor via previously proposed axisymmetrization theories (e.g., Abarca & Montgomery, 2013; Huang et al., 2012; Kepert, 2013; Kepert & Nolan, 2014; Miyamoto et al., 2018; Rozoff et al., 2006; Y. Wang, 2008). Additional case studies and careful modeling studies are needed to further address which hypotheses are best for explaining SEF dynamics. Furthermore, given the implication of the current findings, future work could further examine if these identified asymmetric signals vary in strength and structure for storms experiencing different shear magnitudes.

Appendix:

The asymmetric mode of the K18 model required an asymmetric pressure forcing, which is represented by a nondivergent wind field through a nonlinear balanced relation (see Equation 10 of K18). This appendix describes the procedure that uses the method of optimal interpolation (Daley, 1991) to obtain this asymmetric nondivergent wind field given the eight sector averages of tangential wind composites.

The procedure begins by first applying a low-pass filter to the eight sectors averaged profiles to remove signals of azimuthal wavenumber higher than or equal to 4 (hereafter referred to as the filtered tangential wind field). Given this filtered tangential wind field, the method of optimal interpolation solves for the stream function ψ of the nondivergent wind $\boldsymbol{v}_{\boldsymbol{\psi}}$ (i.e., $\boldsymbol{v}_{\boldsymbol{\psi}} = \left(\partial\psi / \partial r, -1 / r\partial\psi / \partial\lambda\right)$) that minimizes a cost function $J\left(\psi\right)$ of the following form:

$$2J\left(\psi\right) = \left(D_r\psi - v_o\right)^T R^{T/2} O^{-1} R^{1/2} \left(D_r\psi - v_o\right) + \left(-R^{-1}D_\lambda\psi\right)^T R^{T/2} B^{-1} R^{1/2} \left(-R^{-1}D_\lambda\psi\right), \tag{A1}$$

where v_o is the filtered tangential wind; D_r and D_λ are matrix representation of the radial and azimuthal differential operators; R is the radius in a diagonal matrix form; O is the variance of observational uncertainty; B is the variance of uncertainty of the initial guess; T denotes transpose of a matrix. The first term measures the squared distance between the tangential components of the nondivergent wind of the analysis and the observed values, taking into account the uncertainty of the observation, while the second term, on the other hand, measure the squared distance of the radial component. Here, we assume that the observed tangential component of the nondivergent wind is the filtered tangential wind v_o, while the observed nondivergent radial wind is zero. This is a reasonable assumption because the tangential wind is dominated by the nondivergent component, and thus the filtered tangential wind v_o is a good approximation of the observed tangential component of the nondivergent wind. On the other hand, the radial wind is generally an order smaller than the tangential wind component, and is dominated by the irrotational flow associated with the secondary circulation of the TC. An alternative interpretation of the second term is that the analysis begins with an axisymmetric background guess, since the second term essentially measures the asymmetry of the stream function ψ. In this sense, the second term essentially is a regularizer that constrains the magnitude of the asymmetries introduced into the analysis. At the analysis, the solution ψ satisfies $\nabla J\left(\psi\right) = 0$, which yields:

$$\left(D_r\psi - v_o\right)^T R^{T/2} O^{-1} R^{1/2} D_r + \left(-R^{-1}D_\lambda\psi\right)^T R^{T/2} B^{-1} R^{1/2} \left(-R^{-1}D_\lambda\right) = 0 \tag{A2}$$

Rearranging the terms involving ψ to one side yields, and taking transpose of the equation yields:

$$D_r^T R^{T/2} O^{-1} R^{1/2} D_r \psi + \left(R^{-1} D_\lambda^T\right) R^{T/2} B^{-1} R^{1/2} \left(R^{-1} D_\lambda\right) \psi = D_r^T R^{T/2} O^{-1} R^{1/2} v_o \quad \text{(A3)}$$

For simplicity, in this study both O and B are taken to be diagonal (i.e., $O = \mathrm{diag}\left(\sigma_o^2\right)$; $B = \mathrm{diag}\left(\sigma_B^2\right)$), with σ_o^2 having radial and azimuthal dependence and σ_B^2 being a constant. When assuming a diagonal O and B, Equation A3 can be further simplified into the following generalized Poisson equation:

$$\frac{1}{r}\frac{\partial}{\partial r}\left(r\left(\frac{1}{\sigma_o^2}\right)\frac{\partial \psi}{\partial r}\right)+\frac{1}{r^2}\frac{\partial}{\partial \lambda}\left(\frac{1}{\sigma_B^2}\frac{\partial \psi}{\partial \lambda}\right)=\frac{1}{r}\frac{\partial}{\partial r}\left(r\left(\frac{v_o}{\sigma_o^2}\right)\right). \quad \text{(A4)}$$

Equation A4 is similar to the nondivergent component of the typical Helmholtz decomposition, but it further incorporates the information about the variance of observational uncertainty σ_o^2. The information of the variance $\sigma_o^2(r,\lambda)$ can be obtained from the observational composite using a bootstrapping method. At each of the eight azimuthal directions where the quadrant averaging is performed, the set of flight legs within that quadrant are bootstrapped by 1,000 times, and then the variance of the bootstrap mean is computed. After performing this bootstrap procedure for all quadrants, the resulting variance profiles are passed through the same low-pass filter to retain only signals from wavenumber 0–3. On the other hand, since the magnitude of radial wind is typically an order smaller than the tangential component, σ_B^2 is therefore bounded by the value of σ_o^2. For simplicity, σ_B^2 can be taken as the far field value of σ_o^2. Multiple values of σ_B^2 have been tested, and it is found that the magnitude of σ_B^2 only has a small influence on ψ, as well as the simulated updraft response of the K18 model. Therefore, the value of σ_B^2 will be taken to be the azimuthal mean σ_o^2 at $r = 150$ km.

Given v_o, σ_o^2, and σ_B^2, Equation A4 is solved in a circular domain of 300 km radius with a Neumann boundary condition, $\partial\psi / \partial r\,|_{r=300\mathrm{km}} = v_o\left(r = 300\mathrm{km}\right)$ using the method of LU decomposition. The Neumann boundary condition is a natural choice, since it simply implies that the nondivergent tangential wind of the analysis exactly matches with the observed value at the outer boundary.

Data Availability Statement

The FLIGHT+ data set is available at https://verif.rap.ucar.edu/tcdata/flight/. Model output files are available through the DataCommons at Penn State University at https://doi.org/10.26208/2xpf-c686.

Acknowledgments
The authors thank Katharine Wunsch who synthesized the observational data set for this analysis. The authors also thank the anonymous reviewers whose comments led to significant improvements in the manuscript. The Extended Flight Level Data set for Tropical Cyclones (FLIGHT+) was created by the Research Applications Laboratory at the National Center for Atmospheric Research (NCAR) from data provided by the NOAA Hurricane Research Division of AOML and the U.S. Air Force Reserve. The creation of this data set was initially funded through a grant from the Bermuda Institute of Ocean Sciences Risk Prediction Initiative (RPI2.0). NCAR is sponsored by the National Science Foundation. This research was supported by the National Science Foundation under grant AGS-1810869.

References

Abarca, S. F., & Corbosiero, K. L. (2011). Secondary eyewall formation in WRF simulations of hurricanes Rita and Katrina (2005). *Geophysical Research Letters*, *38*, L07802. https://doi.org/10.1029/2011GL047015

Abarca, S. F., & Montgomery, M. T. (2013). Essential dynamics of secondary eyewall formation. *Journal of the Atmospheric Sciences*, *70*, 3216–3230. https://doi.org/10.1175/jas-d-12-0318.1

Abarca, S. F., & Montgomery, M. T. (2014). Departures from axisymmetric balance dynamics during secondary eyewall formation. *Journal of the Atmospheric Sciences*, *71*, 3723–3738. https://doi.org/10.1175/jas-d-14-0018.1

Abarca, S. F., Montgomery, M. T., & McWilliams, J. C. (2015). The azimuthally averaged boundary layer structure of a numerically simulated major hurricane. *Journal of Advances in Modeling Earth Systems*, *7*, 1207–1219. https://doi.org/10.1002/2015ms000457

Bell, M. M., Montgomery, M. T., & Lee, W.-C. (2012). An axisymmetric view of concentric eyewall evolution in Hurricane Rita (2005). *Journal of the Atmospheric Sciences*, *69*, 2414–2432. https://doi.org/10.1175/jas-d-11-0167.1

Black, M. L., & Willoughby, H. E. (1992). The concentric eyewall cycle of Hurricane Gilbert. *Monthly Weather Review*, *120*(2), 947–957. https://doi.org/10.1175/1520-0493(1992)120<0947:tcecoh>2.0.co;2

Chen, G. (2018). Secondary eyewall formation and concentric eyewall replacement in association with increased low-level inner-core diabatic cooling. *Journal of the Atmospheric Sciences*, *75*, 2659–2685. https://doi.org/10.1175/JAS-D-17-0207.1

Chen, G., Wu, C.-C., & Huang, Y.-H. (2018). The role of near-core convective and stratiform heating/cooling in tropical cyclone structure and intensity. *Journal of the Atmospheric Sciences*, *75*, 297–326. https://doi.org/10.1175/jas-d-17-0122.1

Dai, Y., Majumdar, S. J., & Nolan, D. S. (2017). Secondary eyewall formation in tropical cyclones by outflow–jet interaction. *Journal of the Atmospheric Sciences*, *74*, 1941–1958. https://doi.org/10.1175/jas-d-16-0322.1

Daley, R. (1991). *Atmospheric data analysis* (pp. 150–169). Cambridge University Press.

DeMaria, M., Mainelli, M., Shay, L. K., Knaff, J. A., & Kaplan, J. (2005). Further improvements to the Statistical Hurricane Intensity Prediction Scheme (SHIPS). *Weather and Forecasting*, *20*, 531–543. https://doi.org/10.1175/WAF862.1

Didlake, A. C., Jr., Heymsfield, G. M., Reasor, P. D., & Guimond, S. R. (2017). Concentric eyewall asymmetries in Hurricane Gonzalo (2014) observed by airborne radar. *Monthly Weather Review*, *145*, 729–749. https://doi.org/10.1175/mwr-d-16-0175.1

Didlake, A. C., Jr., & Houze, R. A., Jr. (2013). Dynamics of the stratiform sector of a tropical cyclone rainband. *Journal of the Atmospheric Sciences*, *70*, 1891–1911. https://doi.org/10.1175/JAS-D-12-0245.1

Didlake, A. C., Jr., Reasor, P. D., Rogers, R. F., & Lee, W.-C. (2018). Dynamics of the transition from spiral rainbands to a secondary eyewall in Hurricane Earl (2010). *Journal of the Atmospheric Sciences*, *75*, 2909–2929. https://doi.org/10.1175/jas-d-17-0348.1

Fischer, M. S., Rogers, R. F., & Reasor, P. D. (2020). The rapid intensification and eyewall replacement cycles of Hurricane Irma (2017). *Monthly Weather Review*, *148*, 981–1004. https://doi.org/10.1175/mwr-d-19-0185.1

Guimond, S. R., Reasor, P. D., Heymsfield, G. M., & McLinden, M. M. (2020). The dynamics of vortex Rossby waves and secondary eyewall development in Hurricane Matthew (2016): New insights from radar measurements. *Journal of the Atmospheric Sciences*, *77*, 2349–2374. https://doi.org/10.1175/jas-d-19-0284.1

Hawkins, J. D., Helveston, M., Lee, T. F., Turk, F. J., Richardson, K., Sampson, C., et al. (2006). Tropical cyclone multiple eyewall configurations. *Extended Abstracts, 27th Conference on Hurricanes and Tropical Meteorology*. American Meteorological Society, 6B.1.

Hence, D. A., & Houze, R. A., Jr. (2012a). Vertical structure of tropical cyclone rainbands as seen by the TRMM Precipitation Radar. *Journal of the Atmospheric Sciences*, *69*, 2644–2661. https://doi.org/10.1175/jas-d-11-0323.1

Hence, D. A., & Houze, R. A., Jr. (2012b). Vertical structure of tropical cyclones with concentric eyewalls as seen by the TRMM Precipitation Radar. *Journal of the Atmospheric Sciences*, *69*, 1021–1036. https://doi.org/10.1175/jas-d-11-0119.1

Huang, Y.-H., Montgomery, M. T., & Wu, C.-C. (2012). Concentric eyewall formation in Typhoon Sinlaku (2008). Part II: Axisymmetric dynamical processes. *Journal of the Atmospheric Sciences*, *69*, 662–674. https://doi.org/10.1175/jas-d-11-0114.1

Judt, F., & Chen, S. S. (2010). Convectively generated potential vorticity in rainbands and formation of the secondary eyewall in Hurricane Rita of 2005. *Journal of the Atmospheric Sciences*, *67*, 3581–3599. https://doi.org/10.1175/2010jas3471.1

Kepert, J. D. (2001). The dynamics of boundary layer jets within the tropical cyclone core. Part I: Linear theory. *Journal of the Atmospheric Sciences*, *58*, 2469–2484. https://doi.org/10.1175/1520-0469(2001)058<2469:tdoblj>2.0.co;2

Kepert, J. D. (2012). Choosing a boundary layer parameterization for tropical cyclone modeling. *Monthly Weather Review*, *140*, 1427–1445. https://doi.org/10.1175/mwr-d-11-00217.1

Kepert, J. D. (2013). How does the boundary layer contribute to eyewall replacement cycles in axisymmetric tropical cyclones? *Journal of the Atmospheric Sciences*, *70*, 2808–2830. https://doi.org/10.1175/jas-d-13-046.1

Kepert, J. D. (2017). Time and space scales in the tropical cyclone boundary layer, and the location of the eyewall updraft. *Journal of the Atmospheric Sciences*, *74*, 3305–3323. https://doi.org/10.1175/JAS-D-17-0077.1

Kepert, J. D. (2018). The boundary layer dynamics of Tropical cyclone rainbands. *Journal of the Atmospheric Sciences*, *75*, 3777–3795. https://doi.org/10.1175/jas-d-18-0133.1

Kepert, J. D., & Nolan, D. S. (2014). Reply to "Comments on 'How does the boundary layer contribute to eyewall replacement cycles in axisymmetric tropical cyclones?'" *Journal of the Atmospheric Sciences*, *71*, 4692–4704. https://doi.org/10.1175/jas-d-14-0014.1

Kepert, J. D., Schwendike, J., & Ramsay, H. (2016). Why is the tropical cyclone boundary layer not "well mixed"? *Journal of the Atmospheric Sciences*, *73*, 957–973. https://doi.org/10.1175/JAS-D-15-0216.1

Kepert, J. D., & Wang, Y. (2001). The dynamics of boundary layer jets within the tropical cyclone core. Part II: Nonlinear enhancement. *Journal of the Atmospheric Sciences*, *58*, 2485–2501. https://doi.org/10.1175/1520-0469(2001)058<2485:tdoblj>2.0.co;2

Kuo, H. L. (1971). Axisymmetric flows in the boundary layer of a maintained vortex. *Journal of the Atmospheric Sciences*, *28*, 20–41. https://doi.org/10.1175/1520-0469(1971)028<0020:afitbl>2.0.co;2

Li, Q., Wang, Y., & Duan, Y. (2017). A numerical study of outer rainband formation in a sheared tropical cyclone. *Journal of the Atmospheric Sciences*, *74*, 203–227. https://doi.org/10.1088/0953-8984/2/19/00610.1175/jas-d-16-0123.1

Louis, J. F., Tiedtke, M., & Geleyn, J. F. (1982). A short history of the operational PBL parameterization at ECMWF. In *Workshop on planetary boundary layer parameterizations*. European Center for Medium Range Weather Forecasting.

Mellor, G. L., & Yamada, T. (1982). Development of a turbulence closure model for geophysical fluid problems. *Reviews of Geophysics and Space Physics*, *20*, 851–875. https://doi.org/10.1029/rg020i004p00851

Menelaou, K., Yau, M. K., & Martinez, Y. (2012). On the dynamics of the secondary eyewall genesis in Hurricane Wilma (2005). *Geophysical Research Letters*, *39*, L04801. https://doi.org/10.1029/2011GL050699

Miyamoto, Y., Nolan, D. S., & Sugimoto, N. (2018). A dynamical mechanism for secondary eyewall formation in tropical cyclones. *Journal of the Atmospheric Sciences*, *75*, 3965–3986. https://doi.org/10.1175/jas-d-18-0042.1

Montgomery, M. T., & Kallenbach, R. J. (1997). A theory for vortex Rossby-waves and its application to spiral bands and intensity changes in hurricanes. *Quarterly Journal of the Royal Meteorological Society*, *123*, 435–465. https://doi.org/10.1002/qj.49712353810

Qiu, X., & Tan, Z.-M. (2013). The roles of asymmetric inflow forcing induced by outer rainbands in tropical cyclone secondary eyewall formation. *Journal of the Atmospheric Sciences*, *70*, 953–974. https://doi.org/10.1175/jas-d-12-084.1

Qiu, X., Tan, Z.-M., & Xiao, Q. (2010). The role of vortex Rossby waves in hurricane secondary eyewall formation. *Monthly Weather Review*, *138*, 2092–2109. https://doi.org/10.1175/2010mwr3161.1

Rozoff, C. M., Nolan, D. S., Kossin, J. P., Zhang, F., & Fang, J. (2012). The roles of an expanding wind field and inertial stability in tropical cyclone secondary eyewall formation. *Journal of the Atmospheric Sciences*, *69*, 2621–2643. https://doi.org/10.1175/jas-d-11-0326.1

Rozoff, C. M., Schubert, W. H., McNoldy, B. D., & Kossin, J. P. (2006). Rapid filamentation zones in intense tropical cyclones. *Journal of the Atmospheric Sciences*, *63*, 325–340. https://doi.org/10.1175/jas3595.1

Shapiro, L. J., & Willoughby, H. E. (1982). The response of balanced hurricanes to local sources of heat and momentum. *Journal of the Atmospheric Sciences*, *39*, 378–394. https://doi.org/10.1175/1520-0469(1982)039<0378:trobht>2.0.co;2

Sitkowski, M., Kossin, J. P., & Rozoff, C. M. (2011). Intensity and structure changes during hurricane eyewall replacement cycles. *Monthly Weather Review*, *139*, 3829–3847. https://doi.org/10.1175/mwr-d-11-00034.1

Sun, Y. Q., Jiang, Y., Tan, B., & Zhang, F. (2013). The governing dynamics of the secondary eyewall formation of Typhoon Sinlaku (2008). *Journal of the Atmospheric Sciences*, *70*, 3818–3837. https://doi.org/10.1175/jas-d-13-044.1

Tang, X., Tan, Z.-M., Fang, J., Sun, Y. Q., & Zhang, F. (2017). Impact of the diurnal radiation cycle on secondary eyewall formation. *Journal of the Atmospheric Sciences*, *74*, 3079–3098. https://doi.org/10.1175/jas-d-17-0020.1

Terwey, W. D., & Montgomery, M. T. (2008). Secondary eyewall formation in two idealized, full-physics modeled hurricanes. *Journal of Geophysical Research*, *113*, D12112. https://doi.org/10.1029/2007jd008897

Tyner, B., Zhu, P., Zhang, J. A., Gopalakrishnan, S., Marks, F., Jr., & Tallapragada, V. (2018). A top-down pathway to secondary eyewall formation in simulated tropical cyclones. *Journal of Geophysical Research: Atmospheres*, *123*, 174–197. https://doi.org/10.1002/2017jd027410

Vigh, J. L., Dorst, N. M., Williams, C. L., Uhlhorn, E. W., Klotz, B. W., Martinez, J., et al. (2016). FLIGHT+: The extended flight level data set for Tropical Cyclones (Version 1.1). *Tropical cyclone data project*. National Center for Atmospheric Research, Research Applications Laboratory. https://doi.org/10.5065/D6WS8R93

Wang, H., Wang, Y., Xu, J., & Duan, Y. (2019). The axisymmetric and asymmetric aspects of the secondary eyewall formation in a numerically simulated tropical cyclone under idealized conditions on an f plane. *Journal of the Atmospheric Sciences*, *76*, 357–378. https://doi.org/10.1175/jas-d-18-0130.1

Wang, H., Wu, C.-C., & Wang, Y. (2016). Secondary eyewall formation in an idealized tropical cyclone simulation: Balanced and unbalanced dynamics. *Journal of the Atmospheric Sciences*, *73*, 3911–3930. https://doi.org/10.1175/jas-d-15-0146.1

Wang, Y. (2008). Rapid filamentation zone in a numerically simulated tropical cyclone. *Journal of the Atmospheric Sciences*, *65*, 1158–1181. https://doi.org/10.1175/2007JAS2426.1

Willoughby, H. E., Clos, J. A., & Shoreibah, M. G. (1982). Concentric eye walls, secondary wind maxima, and the evolution of the hurricane vortex. *Journal of the Atmospheric Sciences*, *39*(2), 395–411. https://doi.org/10.1175/1520-0469(1982)039<0395:cewswm>2.0.co;2

Willoughby, H. E., Marks, F. D., Jr., & Feinberg, R. J. (1984). Stationary and moving convective bands in hurricanes. *Journal of the Atmospheric Sciences*, *41*, 3189–3211. https://doi.org/10.1175/1520-0469(1984)041<3189:samcbi>2.0.co;2

Wu, C.-C., Huang, Y.-H., & Lien, G.-Y. (2012). Concentric eyewall formation in Typhoon Sinlaku (2008). Part I: Assimilation of T-PARC data based on the Ensemble Kalman Filter (EnKF). *Monthly Weather Review*, *140*, 506–527. https://doi.org/10.1175/MWR-D-11-00057.1

Wunsch, K. E. D., & Didlake, A. C., Jr. (2018). Analyzing tropical cyclone structures during secondary eyewall formation using aircraft in-situ observations. *Monthly Weather Review*, *146*, 3977–3993. https://doi.org/10.1175/mwr-d-18-0197.1

Yu, C.-L., & Didlake, A. C., Jr. (2019). Impact of stratiform rainband heating on the tropical cyclone wind field in idealized simulations. *Journal of the Atmospheric Sciences*, *76*, 2443–2462. https://doi.org/10.1175/jas-d-18-0335.1

Yu, C.-L., Didlake, A. C., Jr., Zhang, F., & Nystrom, R. G. (2021). Asymmetric rainband processes leading to secondary eyewall formation in a model simulation of Hurricane Matthew (2016). *Journal of the Atmospheric Sciences*, *78*, 29–49. https://doi.org/10.1175/jas-d-20-0061.1

Zhang, F., Tao, D., Sun, Y. Q., & Kepert, J. D. (2017). Dynamics and predictability of secondary eyewall formation in sheared tropical cyclones. *Journal of Advances in Modeling Earth Systems*, *9*, 89–112. https://doi.org/10.1002/2016ms000729

Zhang, J. A., Rogers, R. F., Nolan, D. S., & Marks, F. D., Jr. (2011). On the characteristic height scales of the hurricane boundary layer. *Monthly Weather Review*, *139*, 2523–2535. https://doi.org/10.1175/mwr-d-10-05017.1

Zhang, J. A., Rogers, R. F., Reasor, P., Uhlhorn, E., & Marks, F. D., Jr. (2013). Asymmetric hurricane boundary layer structure from dropsonde composites in relation to the environmental wind shear. *Monthly Weather Review*, *141*, 3968–3984. https://doi.org/10.1175/MWR-D-12-00335.1

Zhu, P., Zhu, Z., Gopalakrishnan, S., Black, R., Marks, F. D., Tallapragada, V., et al. (2015). Impact of subgrid-scale processes on eyewall replacement cycle of tropical cyclones in HWRF system. *Geophysical Research Letters*, *42*, 10027–10036. https://doi.org/10.1002/2015GL066436